FACULDADE DE ENGENHARIA DA UNIVERSIDADE DO PORTO

FEUP

The Material Non Linear Analysis of 2D Structures Using a Radial Point Interpolation Method

Henrique Manuel Sousa Duarte

Mestrado Integrado em Engenharia Mecânica

Supervisor: Jorge Belinha (Post-PhD Researcher and Invited Auxiliar Professor)

Co-Supervisor: Renato M. Natal Jorge (Associated Professor)

Co-Supervisor: Lúcia M. J. S. Dinis (Associated Professor)

July 2014

The Material Non Linear Analysis of 2D Structures Using a Radial Point Interpolation Method

Henrique Manuel Sousa Duarte

Mestrado Integrado em Engenharia Mecânica

July 2014

Agradecimentos

Em primeiro lugar, gostaria de agradecer ao Professor Jorge Belinha, orientador. Obrigado por ter despertado o meu interesse pelo estudo dos métodos sem malha. Obrigado pela disponibilidade que demonstrou ao longo da realização desta tese, assim como ao longo dos trabalhos e apresentações que a precederam.

Ao Professor Renato Natal Jorge e Professora Lúcia Dinis, agradeço a oportunidade que me foi dada para entrar no mundo da investigação. O convite pessoal e a visita guiada aos diferentes projetos em desenvolvimento ficarão para sempre gravados na minha memória como um dos momentos altos do meu percurso académico.

Aos colegas de curso e amigos José Andrade, Rafael Tavares, João Ferreira, Francisco Rua, Tiago Ramos, entre muitos outros, agradeço todo o tempo passado em grupo, quer em ambiente sério e de trabalho, quer nos momentos de descontração.

À minha família, em particular aos meus pais e padrinhos, o meu profundo agradecimento pelo apoio incondicional ao longo deste trabalho e de todo o percurso até ele. Obrigado por criarem todas as condições necessárias para que fosse bem sucedido. Obrigado pelo incentivo e ânimo constantes.

Finalmente, gostaria de agradecer a todos os que, de uma forma ou de outra, me ajudaram na realização deste trabalho.

Abstract

In this work, the Radial Point Interpolation Method (RPIM) is used to study several solid mechanics problems, starting with elastic benchmark examples, then elastoplastic problems, with monotonic and non monotonic loading conditions. Additionally, examples of trabecular and cortical bone are analysed.

Meshless methods have been the focus of interest in the past few years, mainly because of the advantages they have when compared to the well known and established Finite Element Method. Some of these advantages are the production of smoother stress fields and the more flexible discretization technique.

In the RPIM, the nodal connectivity is imposed using the concept of neighbour nodes, which are radially searched around the interest node. This creates variable sized influence domains that contain the neighbour nodes of the interest node, and that are used to create the interpolation functions.

The RPIM is not a trully meshless method, since a background mesh is required to perform the numerical integration of the interpolation functions. This mesh can be fitted to the domain of the problem or blindly regular, with the subsequent exclusion of integration points outside the domain.

The interpolation functions used in the RPIM contain a polynomial basis and a radial basis. The Radial Basis Function (RBF) used in this work is the Multiquadric RBF. Since the interpolation functions possess the delta Kronecker property, the imposition of natural and essencial boundary conditions is simple and direct.

Regarding the non-linear analysis, small deformations and elastoplastic material behaviour are considered. In order to solve the non-linear equation system, an incremental and iterative method is used, a modified Newton-Raphson method. In the initial stiffnes method (KT0), the stiffness matrix is calculated only once at the start of the analysis, which reduced the computational cost, but increases the number of iterations. The yield criterion used for the non-linear analysis is the Von Mises criterion, and the forward-Euler procedure is used to return the stresses to the yield surface.

Several linear elastic benchmark examples are solved, in order to assess the quality of the meshless method. After that, non-linear examples are analysed, first with monotonic loading and then with non monotonic loading. The final application is the study of the trabecular and cortical bone using elastoplastic material behaviour. The obtained results suggest that the RPIM is an accurate and reliable meshless method.

Resumo

Neste trabalho, o "Radial Point Interpolation Method" (RPIM) é usado no estudo de diversos problemas de mecânica dos sólidos, começando com exemplos lineares de referência, passando depois para problemas não lineares, com cargas monotónicas e não monotónicas. Álem disso, exemplos de osso trabecular e cortical são analisados.

Os métodos sem malha têm sido o foco da atenção nos últimos anos, principalmente devido às vantagens que apresenta quando comparado com o conhecido e estabelecido Método dos Elementos Finitos. Algumas destas vantangens são a produção de campos de tensões suaves e maior flexibilidade de discretização.

No RPIM, a conetividade nodal é imposta usando o conceito de nós vizinhos, que são radialmente procurados à volta do nó de interesse. Assim são criados domínios de influência de tamanho variável que contêm os nós vizinhos do nó de interesse, usados para a criação das funções de interpolação.

O RPIM não é um método sem malha puro, uma vez que é necessária a criação de uma malha de fundo para a integração numérica das funções interpoladoras. A malha pode ser ajustada ao modelo ou regular, sendo necessário neste caso a remoção posterior dos pontos de integração fora do domínio.

As funções de interpolação usadas no RPIM são formadas por uma base polinomial e por uma base radial. A base radial usada neste trabalho é a multiquadrica. Uma vez que as funções de forma possuem a propriedade de delta Kronecker, a imposição das condições de fronteira naturais e essenciais é simples e direta.

No que diz respeito à análise não linear, foram consideradas pequenas deformações e comportamento material elastoplástico. De forma a resolver o sistema de equações não linear, é usado um método incremental e iterativo, o método de Newton-Raphson modificado. No método de rigidez inicial (KT0), a matriz de rigidez é calculada apenas uma vez no início da análise, o que reduz o custo computacional mas aumenta o número de iterações. O critério de cedência usado para a análise não linear é o critério de Von Mises, e o processo "forward-Euler" é utilizado para retornar as tensões à superfície de cedência.

Vários exemplos lineares de referência são resolvidos, de forma a avaliar a qualidade do método sem malha. Depois disso, são analisados exemplos não lineares, primeiro com cargas monotónicas e depois com cargas não monotónicas. A última aplicação é o estudo do osso trabecular e cortical utilizando comportamento material elastoplástico. Os resultados obtidos sugerem que o RPIM é um método sem malha preciso e fiável.

Contents

List of Figures

Chapter 1

Introduction

The engineering design process can be divided in a series of different specific phases. The present work focus on three of those phases: the Modulation, the Simulation and the Analysis. A meshless method is applied to an elastoplastic analysis. The Radial Point Interpolation Method is the method used.

1.1 Meshless Methods

In the recent past, meshless methods have been subject to great developments, which made them an alternative to the well known finite element methods (FEM) [1, 2]. The main difference from these two methods is the discretization process. In meshless methods, the domain is discretized in an arbitrary set of nodes, as opposed to FEM, where the domain is discretized in an element mesh. This means that in the meshless methods, the influence domain is not restricted to a single element.

One of the first meshless methods, the smooth particle hydrodynamics (SPH) [3, 4], was initially used to model some astrophysical phenomena [5]. The method was extend by Libersky and Petschek [6] with the intent of solving solid mechanics problems using a strong formulation.

Some other meshless methods have been developed since the SPH, specifically seeking the weak form solution. One of the first of this kind, the element free Galerkin (EFG) [7], uses the moving least-squares approximants (MLS), developed by Lancaster and Salkauskas [8]. Parallelly, the reproducing kernel particle method (RKPM) was developed [9], along with the meshless local Petrov-Galerking (MLPG) method [10], one of the most famous weak formulation based meshless method.

Unfortunately, all of the methods mentioned earlier use approximation functions, which do not possess the delta Kronecker property. Therefore, the treatment of the natural and essential boundary conditions is harder than the treatment when interpolation functions are used [4, 11, 12].

In the last few years, many meshless methods using interpolation functions have been developed, with the main goal of making the imposition of the natural and essential boundary conditions easier. The main ones are the Point Interpolation Method (PIM) [13, 14], the Radial Point Interpolation Method (RPIM) [15, 16], the Natural Neighbour Finite Element Method (NNFEM) [17, 18], the Meshless Finite Element Method (MFEM) [19] and more recently the Radial Natural Element Method (NREM) [20, 21].

1.2 Objective

The main objective of this work is the analysis of elastoplastic materials. For this, an existing MATLAB code [22] was studied, and additional code was created in order to perform the non linear analysis. The code includes the KT0 algorithm, the stress return algorithm and the analysis of non monotonic loads.

1.3 Thesis Structure

The structure of this work is described as follows. In Chapter 2, the meshless method used in this work, the RPIM, is presented. Chapter 3 presents the elastic and elastoplastic mechanical fundamentals. The nonlinear solution algorithm and the stress return algorithm used to solve elastoplastic problems are described in Chapter 4. Chapter 5 presents the analysis of linear elastic problems, in order to evaluate the performance of the meshless method used. In Chapter 6, the analysis of some benchmark nonlinear problems is presented, along with the study of some non monotonic loading cases. In addition, the example of the trabecular bone and polymer analogue material is analysed, as well as the cortical bone case. Finally, in Chapter 7 the main conclusions of this work are presented, along with perspectives for future works.

Chapter 2

Meshless Method

In the past few years, meshless methods have come into focus of interest, specially in the engineering community. Their development is related to the need to overcome some limitations found in the finite element methods (FEM).

In the meshless methods, the nodes can be arbitrarily distributed inside the domain, since the field functions (such as displacement and stresses) are approximated within an influence domain, rather than an element [2, 4, 23]. These influence domains may and must overlap, as opposed to FEM, in which there is a no-overlap rule between elements [24, 25].

In this chapter, the Radial Point Interpolation Method (RPIM) is presented.

2.1 Radial Point Interpolators

The Radial Point Interpolators (RPI) have their origin in the Point Interpolation Method (PIM) [13]. In this method, polynomial interpolants possessing the delta Kronecker property are constructed, based only on a group of arbitrarily distributed points. This technique, however, has several numerical problems, for example the perfect alignment of the nodes produces a singular solution in the interpolation functions.

To overcome these problems, a radial basis function was introduced in the construction process of the interpolation functions to stabilize the method, and the PIM evolved to the Radial Point Interpolation Method (RPIM) [15].

The RPIM was initially developed to perform data surface fitting. Later, Kansa's developments [26] to the RBF allowed it to be used for diferential equation solving. Unlike Kansa's algorithm, which uses the concept "global domain", the RPIM uses the "influence domain". This generates sparse and banded stiffness matrices, more adequate to complex geometry problems.

2.2 Influence Domain and Nodal Connectivity

Consider a problem domain Ω, bounded by Γ, discretized in a set of randomly placed nodes $N = \{n_0, n_1, \ldots, n_N\} \in \mathbb{R}^2$, as shown in figure 2.1.

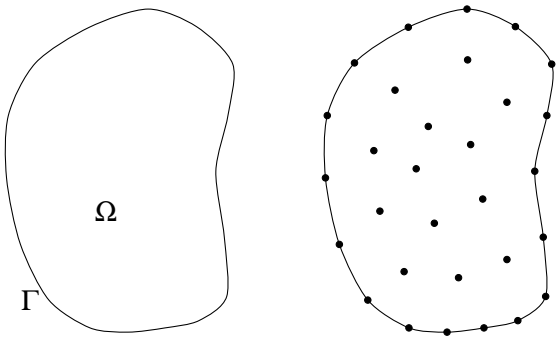

Figure 2.1: Discretization of the Problem Domain in Several Randomly Distributed Nodes

In early works, the nodal connectivity in the RPIM is obtained by overlaping the influence domains of the nodes [13, 14]. These domains are constructed by searching nodes inside a fixed area (or a fixed volume).

This concept is very simple, however the irregular boundaries or different node densities inside the model can lead to unbalanced influence domains. It would be ideal if the influence domains in the problem contained the same number of nodes [22].

The solution to this problem is the use of a variable influence domain. Instead of a fixed size, this influence domain has a fixed number of nodes n, while the size may vary, as shown in figure 2.2. For each interest point, a radial search around the point itself is performed, and the n closest nodes are defined.

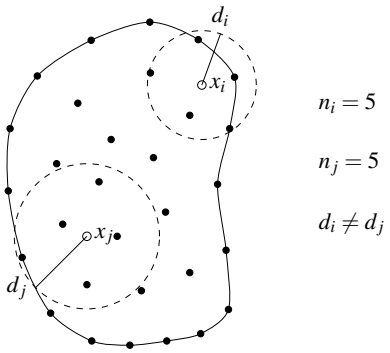

Figure 2.2: Variable Influence Domain

Previous work [27] suggests that the number of nodes inside each influence domain should vary between $n \in [16, 25]$.

2.3 Numerical Integration

In the present work, the Gauss-Legendre integration scheme is considered.

The solid domain is divided in a regular grid, and each grid cell is filled with integration points, respecting the Gauss-Legendre quadrature rule. Figure 2.3 shows an example for a single cell.

The initial quadrilateral cell (figure 2.3(a)) is transformed in an isoparametric square (figure 2.3(b)). The Gauss-Legendre quadrature points are placed inside the isoparametric square. In this case, as in the whole work, a 2×2 quadrature is used.

The cartesian coordinates of the integration points are obtained by using the isoparametric interpolation functions (figure 2.3(c)). The weight of each integration point is the product of the isoparametric weight and the determinant of the Jacobian matrix's inverse for the respective cell [22].

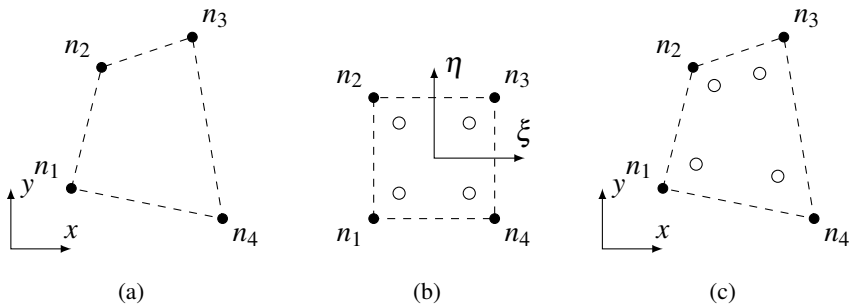

Figure 2.3: Gauss-Legendre Integration [22]: (a) Initial Cell; (b) Transformation of the Initial Cell in an Isoparametric Square and Application of 2×2 Quadrature Rule; (c) Return to the Initial Cell.

If the solid domain is fairly regular, a regular integration mesh that fits the domain can be constructed, and no additional post-treatment is required (figure 2.4(a)). Although, if the domain is irregular, a regular mesh can be created, as figure 2.4(b) shows, and after the integration points are placed, the ones that are outside the domain are removed.

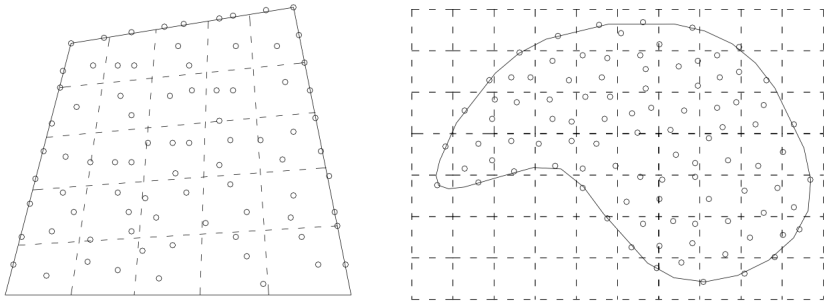

Figure 2.4: Background Integration Mesh [22]: (a) Fitted Mesh; (b) Regular Blind Mesh.

Consider the function $\boldsymbol{F}(x)$ defined in the domain Ω. The numerical integration can be expressed by,

$$\int_{\Omega} \boldsymbol{F}(x)\, d\Omega = \sum_{i=1}^{n_g} \widehat{w}_i \boldsymbol{F}(x_i) \tag{2.1}$$

where $\widehat{w}_i$ is the weight of the integration point x_i.

2.4 Interpolation Functions

In this work, the punctual radial type functions - RPI (radial point interpolators) are used [11, 15].

Consider a function $\boldsymbol{u}(\boldsymbol{x})$, defined in the domain Ω, discretized by a set of N nodes. It is assumed that only the nodes inside the influence domain of the interest point $\boldsymbol{x}_I$ have effect on the function $\boldsymbol{u}(\boldsymbol{x})$. Using a radial basis function, the function $\boldsymbol{u}(\boldsymbol{x})$ passes through all the nodes of the influence domain.

The value of the function $\boldsymbol{u}(\boldsymbol{x})$ at the interest point $\boldsymbol{x}_I$ is obtained by,

$$\boldsymbol{u}(\boldsymbol{x}_I) = \sum_{i=1}^{n} R_i(\boldsymbol{x}_I)\, a_i(\boldsymbol{x}_I) + \sum_{j=1}^{m} p_j(\boldsymbol{x}_I)\, b_j(\boldsymbol{x}_I) = \left\{\boldsymbol{R}^T(\boldsymbol{x}_I), \boldsymbol{p}^T(\boldsymbol{x}_I)\right\} \begin{Bmatrix} \boldsymbol{a} \\ \boldsymbol{b} \end{Bmatrix} \tag{2.2}$$

where $R_i(\boldsymbol{x}_I)$ is the RBF and n is the number of nodes inside the influence domain of the interest point $\boldsymbol{x}_I$. The coefficients $a_i(\boldsymbol{x}_I)$ and $b_i(\boldsymbol{x}_I)$ are, respectively, non constant coefficients of $R_i(\boldsymbol{x}_I)$ and $p_j(\boldsymbol{x}_I)$.

The monomials of the polynomial basis are defined by $p_j(\boldsymbol{x}_I)$ and m is the basis monomial number. The vectors of equation 2.2 are defined as,

$$\boldsymbol{R}^T(\boldsymbol{x}_I) = \{R_1(\boldsymbol{x}_I), R_2(\boldsymbol{x}_I), \ldots, R_n(\boldsymbol{x}_I)\} \tag{2.3}$$

$$\boldsymbol{p}^T(\boldsymbol{x}_I) = \{p_1(\boldsymbol{x}_I), p_2(\boldsymbol{x}_I), \ldots, p_m(\boldsymbol{x}_I)\} \tag{2.4}$$

$$\boldsymbol{a}^T(\boldsymbol{x}_I) = \{a_1(\boldsymbol{x}_I), a_2(\boldsymbol{x}_I), \ldots, a_n(\boldsymbol{x}_I)\} \tag{2.5}$$

$$\boldsymbol{b}^T(\boldsymbol{x}_I) = \{b_1(\boldsymbol{x}_I), b_2(\boldsymbol{x}_I), \ldots, b_m(\boldsymbol{x}_I)\} \tag{2.6}$$

Several known RBF's are well studied and developed [15, 28]. In this work, the Multiquadric (MQ) function is used, initially proposed by Hardy [29]. The MQ-RBF is defined as,

$$R(r_{Ii}) = \left(r_{Ii}^2 + c^2\right)^p \tag{2.7}$$

where c and p are two shape parameters that require an optimization study, since the variation of these parameters greatly affects the performance of the RBF. Previous work suggests that $c \cong 0$ and $p \cong 1$ [11, 30]. The variable of the RBF is the Euclidian norm r_{Ii}, which defines the distance between the interest point $\boldsymbol{x}_I$ and the neighbour node $\boldsymbol{x}_i$,

$$r_{ij} = \sqrt{(x_I - x_i)^2 + (y_I - y_i)^2} \tag{2.8}$$

The polinomial basis added must be complete to assure that the interpolation of the RBF matrix is invertible [11]. The polinomial basis that can be used for the two-dimensional space are,

$$\text{Null Basis - } \boldsymbol{x}^T = \{x,y\}; \quad \boldsymbol{p}^T(\boldsymbol{x}) = \{0\}; \quad m = 0, \tag{2.9}$$

$$\text{Constant Basis - } \boldsymbol{x}^T = \{x,y\}; \quad \boldsymbol{p}^T(\boldsymbol{x}) = \{1\}; \quad m = 1, \tag{2.10}$$

$$\text{Linear Basis - } \boldsymbol{x}^T = \{x,y\}; \quad \boldsymbol{p}^T(\boldsymbol{x}) = \{1,x,y\}; \quad m = 3, \tag{2.11}$$

$$\text{Quadratic Basis - } \boldsymbol{x}^T = \{x,y\}; \quad \boldsymbol{p}^T(\boldsymbol{x}) = \left\{1,x,y,x^2,xy,y^2\right\}; \quad m = 6. \tag{2.12}$$

In this work, the constant polinomial basis is used.

There is an additional requirement that the polinomial basis must satisfy in order to obtain a unique solution [11],

$$\sum_{i=1}^{n} p_j(x_i)\, a_i(x_i) = 0, \quad j = 1,2,\ldots,m \tag{2.13}$$

Therefore, a new equation system can be defined,

$$\left\{ \begin{array}{c} \boldsymbol{u}_s \\ \boldsymbol{0} \end{array} \right\} = \boldsymbol{G} \left\{ \begin{array}{c} \boldsymbol{a} \\ \boldsymbol{b} \end{array} \right\} \tag{2.14}$$

where $\boldsymbol{G}$ is a matrix defined by,

$$\boldsymbol{G} = \left[\begin{array}{cc} \boldsymbol{R}_Q & \boldsymbol{P}_m \\ \boldsymbol{P}_m^T & \boldsymbol{0} \end{array} \right] \tag{2.15}$$

being $\boldsymbol{R}_Q$ the moment matrix of the RBF,

$$\boldsymbol{R}_Q = \left[\begin{array}{cccc} R(r_{11}) & R(r_{12}) & \cdots & R(r_{1n}) \\ R(r_{21}) & R(r_{22}) & \cdots & R(r_{2n}) \\ \vdots & \vdots & \ddots & \vdots \\ R(r_{n1}) & R(r_{n2}) & \cdots & R(r_{nn}) \end{array} \right] \tag{2.16}$$

and $\boldsymbol{P}_m$ the moment matrix of the polynomial basis,

$$\boldsymbol{P}_m = \left[\begin{array}{cccc} P_1(x_1) & P_2(x_1) & \cdots & P_m(x_1) \\ P_1(x_2) & P_2(x_2) & \cdots & P_m(x_2) \\ \vdots & \vdots & \ddots & \vdots \\ P_1(x_n) & P_2(x_n) & \cdots & P_m(x_n) \end{array} \right] \tag{2.17}$$

Solving equation 2.14,

$$\left\{ \begin{array}{c} \boldsymbol{a} \\ \boldsymbol{b} \end{array} \right\} = \boldsymbol{G}^{-1} \left\{ \begin{array}{c} \boldsymbol{u}_s \\ \boldsymbol{0} \end{array} \right\} \tag{2.18}$$

Substituting the previous equation in the interpolation function (equation 2.2),

$$\boldsymbol{u}(\boldsymbol{x}_I) = \left\{ \boldsymbol{R}^T(\boldsymbol{x}_I), \boldsymbol{p}^T(\boldsymbol{x}_I) \right\} \boldsymbol{G}^{-1} \left\{ \begin{array}{c} \boldsymbol{u}_s \\ \boldsymbol{0} \end{array} \right\} = \varphi(\boldsymbol{x}_I) \boldsymbol{u}_s \tag{2.19}$$

where $\varphi(\boldsymbol{x})$ is the interpolation function defined as,

$$\varphi(\boldsymbol{x}_I) = \left\{ \boldsymbol{R}^T(\boldsymbol{x}_I), \boldsymbol{p}^T(\boldsymbol{x}_I) \right\} \boldsymbol{G}^{-1} = \left\{ \varphi_1(\boldsymbol{x}_I), \varphi_2(\boldsymbol{x}_I), \ldots, \varphi_n(\boldsymbol{x}_I) \right\} \tag{2.20}$$

Figure 2.5 shows a schematic representation of the interpolation functions for a one-dimensional space [31]. It is visible that the functions have a null value on all nodes of the influence domain except the interest point $\boldsymbol{x}_I$. The interpolation function has a unit value for this point. Therefore, the RPIM function possesses the delta Kronecker property. Its derivatives are easily obtainable [11, 30, 32].

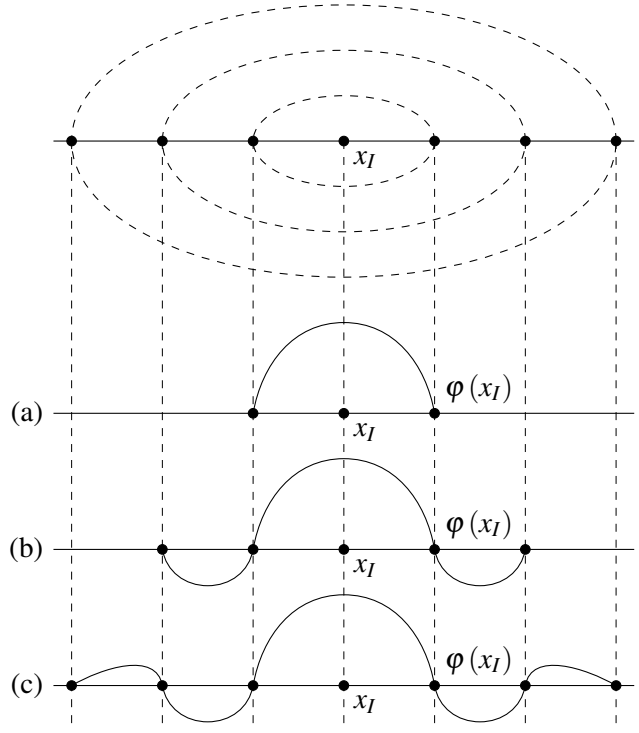

Figure 2.5: Interpolation Functions for a One-Dimensional Space: (a) 2 Node Influence Domain; (b) 4 Node Influence Domain; (c) 6 Node Influence Domain [31]

Chapter 3

Mechanical Fundamentals

The science of solid mechanics is the foundation for the modelling and designing of structural systems. It defines the relations between stresses (which are used to verify how far the structure is from yielding), and strains (caused by the loading conditions of the structure) [33].

In relation to mechanical properties, materials can be divided in two groups. Isotropic materials have the same mechanical properties in all directions, as oposed to anisotropic materials, in which the mechanical properties vary depending on the direction. The first group can be defined by two independent material constants (usually the Young's modulus and the Poisson's ratio). For the second group, multiple constants may be required, depending on the level of anisotropy (transversely isotropic, orthotropic) [34].

Regarding the relationship between deformation and force aplied to a solid, materials can be defined as elastic (the deformation disappears when the solid is unloaded) or plastic (the deformation in the solid can't be fully recovered after unloading). In this work, both cases are considered.

The boundary conditions are an important consideration in solid mechanics [33, 34]. These can be applied through forces or imposed displacements. In this work, only static (or quasistatic) forces are considered, which means the stress, strain and displacement will not be a function of time.

3.1 Problem Formulation

3.1.1 Displacement Field

Consider a two dimenionsal problem, where the domain Ω is bounded by Γ. In case of the application of an external force, the points in domain Ω will change to the domain Ω'. Figure 3.1 shows the initial particle P moving to position P' [35].

The vector $\boldsymbol{u}(u,v)$ represented in figure 3.1 is a function of the coordinates (x,y), as shown in equation 3.1. It represents the displacement field for the two dimensional body.

$$\boldsymbol{u}(u,v) = \left\{ \begin{array}{c} u(x,y) \\ v(x,y) \end{array} \right\} \tag{3.1}$$

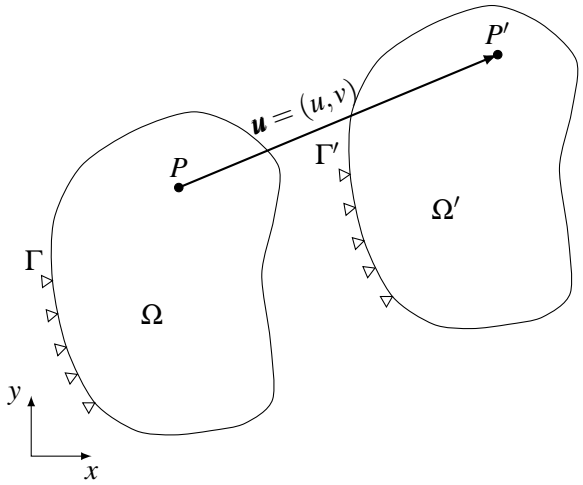

Figure 3.1: Displacement Field

3.1.2 Strain Field

Strain is a measure of deformation, which can be caused by external loads, body forces or internal forces, such as the ones caused by temperature gradients. It can be defined as the change of displacement per unit length.

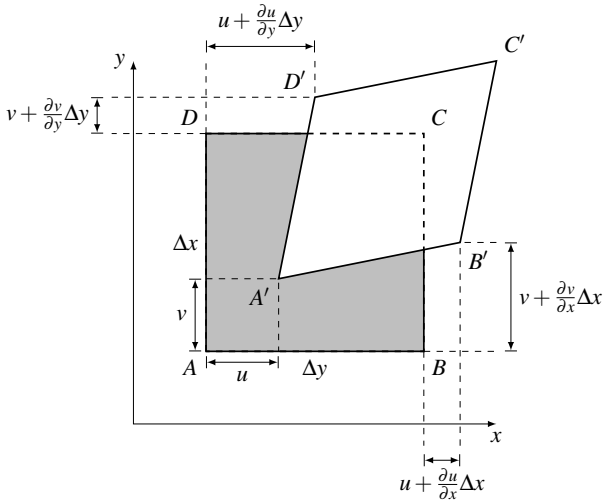

Figure 3.2: Cartesian Components of Strain for an Infinitesimal Material Element

Strains can be divided into normal strains (related to dilatations or contractions) or shear strains (related to distortions).

Figure 3.2 represents the strain field components (normal and shear strain) for the two dimensional material element.

The strain matrix can be defined by equation 3.2,

$$\boldsymbol{\varepsilon} = \begin{bmatrix} \varepsilon_{xx} & \varepsilon_{xy} \\ \varepsilon_{yx} & \varepsilon_{yy} \end{bmatrix} \tag{3.2}$$

where the normal strains are given by,

$$\varepsilon_{xx} = \frac{\partial u}{\partial x} \quad ; \quad \varepsilon_{yy} = \frac{\partial v}{\partial y} \tag{3.3}$$

and the shear strain by (note that $\gamma_{ij} = 2 \times \varepsilon_{ij}$),

$$\gamma_{xy} = \gamma_{yx} = \frac{\partial u}{\partial y} + \frac{\partial v}{\partial x} \tag{3.4}$$

Since the strain matrix is symmetric, the Voigt notation can be implemented, turning equation 3.2 into,

$$\boldsymbol{\varepsilon} = \begin{Bmatrix} \varepsilon_{xx} \\ \varepsilon_{yy} \\ \varepsilon_{xy} \end{Bmatrix} \tag{3.5}$$

Replacing equations 3.3 and 3.4 in the previous one gives,

$$\boldsymbol{\varepsilon} = \begin{Bmatrix} \varepsilon_{xx} \\ \varepsilon_{yy} \\ \varepsilon_{xy} \end{Bmatrix} = \begin{Bmatrix} \frac{\partial u}{\partial x} \\ \frac{\partial v}{\partial y} \\ \frac{\partial u}{\partial y} + \frac{\partial v}{\partial x} \end{Bmatrix} \tag{3.6}$$

Equation 3.6 can be represented as a product of a partial differential operator $\boldsymbol{L}$ and the displacement vector $\boldsymbol{u}$,

$$\boldsymbol{\varepsilon} = \boldsymbol{L} \cdot \boldsymbol{u} = \begin{bmatrix} \frac{\partial}{\partial x} & 0 \\ 0 & \frac{\partial}{\partial y} \\ \frac{\partial}{\partial y} & \frac{\partial}{\partial x} \end{bmatrix} \cdot \begin{Bmatrix} u \\ v \end{Bmatrix} \tag{3.7}$$

3.1.3 Constitutive Equations

When dealing with elastic materials, the constitutive equation that expresses the relationship between stresses and strains is the Hooke's Law, given by,

$$\boldsymbol{\sigma} = \boldsymbol{c} \cdot \boldsymbol{\varepsilon} \tag{3.8}$$

where $\boldsymbol{c}$ is the material matrix. This material matrix is composed of several material constants, obtained by experimental tests.

Hooke's Law (equation 3.8) can be written in an explicit way as,

$$\begin{Bmatrix} \sigma_{xx} \\ \sigma_{yy} \\ \sigma_{zz} \\ \gamma_{xy} \\ \gamma_{yz} \\ \gamma_{zx} \end{Bmatrix} = \begin{bmatrix} C_{11} & C_{12} & C_{13} & C_{14} & C_{15} & C_{16} \\ & C_{22} & C_{23} & C_{24} & C_{25} & C_{26} \\ & & C_{33} & C_{34} & C_{35} & C_{36} \\ & & & C_{44} & C_{45} & C_{46} \\ & sym & & & C_{55} & C_{56} \\ & & & & & C_{66} \end{bmatrix} \begin{Bmatrix} \varepsilon_{xx} \\ \varepsilon_{yy} \\ \varepsilon_{zz} \\ \gamma_{xy} \\ \gamma_{yz} \\ \gamma_{zx} \end{Bmatrix} \tag{3.9}$$

which means that, for a three dimensional problem, there are twenty one independent material constants to be defined (for the case of a full anisotropic material).

In the case of an orthotropic material (with three orthogonal planes of symmetry) the $\boldsymbol{c}$ matrix is given by,

$$\boldsymbol{c}^{-1} = \boldsymbol{s} = \begin{bmatrix} \frac{1}{E_{xx}} & -\frac{\nu_{yx}}{E_{yy}} & -\frac{\nu_{zx}}{E_{zz}} & 0 & 0 & 0 \\ -\frac{\nu_{xy}}{E_{xx}} & \frac{1}{E_{yy}} & -\frac{\nu_{zy}}{E_{zz}} & 0 & 0 & 0 \\ -\frac{\nu_{xz}}{E_{xx}} & -\frac{\nu_{yz}}{E_{yy}} & \frac{1}{E_{zz}} & 0 & 0 & 0 \\ 0 & 0 & 0 & \frac{1}{G_{yz}} & 0 & 0 \\ 0 & 0 & 0 & 0 & \frac{1}{G_{xz}} & 0 \\ 0 & 0 & 0 & 0 & 0 & \frac{1}{G_{xy}} \end{bmatrix} \tag{3.10}$$

This matrix is obtained from the inverse of the compliance matrix $\boldsymbol{s}$.

In the previous equation, E_{ii} is the Young's modulus in direction i, which measures the stiffness of the masterial, ν_{ij} is the Poisson's ratio. This ratio represents the relation between the lateral contraction of the material in direction i and the elongation along j, when a uniaxial stress is apllied along j. Finally, G_{ij} is the shear modulus.

In conclusion, an orthotropic material requires nine independent materials constants.

If an isotropic material is considered, the material matrix is even simpler,

$$\boldsymbol{c} = \frac{E}{(1-2\nu)(1+\nu)} \begin{bmatrix} 1-\nu & \nu & \nu & 0 & 0 & 0 \\ \nu & 1-\nu & \nu & 0 & 0 & 0 \\ \nu & \nu & 1-\nu & 0 & 0 & 0 \\ 0 & 0 & 0 & G & 0 & 0 \\ 0 & 0 & 0 & 0 & G & 0 \\ 0 & 0 & 0 & 0 & 0 & G \end{bmatrix} \tag{3.11}$$

where the shear modulus G is defined as a function of E and ν,

$$G = \frac{E}{2(1+\nu)} \tag{3.12}$$

Therefore, only two independent material constants are required to define an isotropic material.

3.2 Weak Form

The strong form equation system is the differential equation system governing the studied physical phenomenon. The weak form, by contrast, requires a weaker consistency of the approximation (or interpolator) functions used. The ideal situation would be obtaining the exact solution for a equation system through the strong form. However, it is extremely difficult to generalize the strong form for complex engineering problems. Weak form based formulations are able to produce a stable algebric equation system that leads to more accurate results. Therefore, the most used formulation is the weak form.

The principles used to define the weak forms in the Finite Element Method can also be used in the RPIM [24, 36, 37].

In this work, the discrete equation system is obtained by using the Galerking weak form, which is a variational method [37].

3.2.1 Weak Form of Galerkin

The Galerkin's weak form is a variational method based on an energetic principle [22]. Of all the displacement configurations that sastify the compatibility and boundary conditions, as well as the initial and final time conditions, the configuration that corresponds to the real solution is the one which minimizes the Lagrangian functional L,

$$\delta \int_{t_1}^{t_2} L dt = 0$$

being the Lagrangian funtional L defined as,

$$L = T - \Pi + W_f \tag{3.14}$$

where T is the kinetic energy, Π is the strain energy and W_f the work produced by the external forces.

The kinetic energy is defined as,

$$T = \frac{1}{2} \int_{\Omega} \rho \dot{\boldsymbol{u}}^T \dot{\boldsymbol{u}} d\Omega \tag{3.15}$$

where Ω is the body volume, ρ is the mass density and $\dot{\boldsymbol{u}}$ is the first derivative of the displacement, i.e. the velocity.

The strain energy, for elastic materials, is defined as,

$$\Pi = \frac{1}{2} \int_{\Omega} \boldsymbol{\varepsilon}^T \boldsymbol{\sigma} d\Omega \tag{3.16}$$

being $\boldsymbol{\varepsilon}$ the strain vector and $\boldsymbol{\sigma}$ the stress vector. The work produced by the external forces can be expressed as,

$$W_f = \int_\Omega \boldsymbol{u}^T \boldsymbol{b} d\Omega + \int_{\Gamma_t} \boldsymbol{u}^T \bar{\boldsymbol{t}} d\Gamma \tag{3.17}$$

where $\boldsymbol{u}$ is the displacement field, $\boldsymbol{b}$ the body force vector and Γ_t is the traction boundary where the external forces $\bar{\boldsymbol{t}}$ are applied.

The Lagrangian functional can now be rewritten as,

$$L = \frac{1}{2}\int_\Omega \rho \dot{\boldsymbol{u}}\dot{\boldsymbol{u}} d\Omega - \frac{1}{2}\int_\Omega \boldsymbol{\varepsilon}^T \boldsymbol{\sigma} d\Omega + \int_\Omega \boldsymbol{u}^T \boldsymbol{b} d\Omega + \int_{\Gamma_t} \boldsymbol{u}^T \bar{\boldsymbol{t}} d\Gamma \tag{3.18}$$

Minimizing the Lagrangian functional,

$$\delta \int_{t_1}^{t_2} \left(\frac{1}{2}\int_\Omega \rho \dot{\boldsymbol{u}}\dot{\boldsymbol{u}} d\Omega - \frac{1}{2}\int_\Omega \boldsymbol{\varepsilon}^T \boldsymbol{\sigma} d\Omega + \int_\Omega \boldsymbol{u}^T \boldsymbol{b} d\Omega + \int_{\Gamma_t} \boldsymbol{u}^T \bar{\boldsymbol{t}} d\Gamma \right) dt = 0 \tag{3.19}$$

In this work, only static problems are studied. Therefore the kinetic energy is always null, and the previous equation can be simplified,

$$\delta \int_{t_1}^{t_2} \left(-\frac{1}{2}\int_\Omega \boldsymbol{\varepsilon}^T \boldsymbol{\sigma} d\Omega + \int_\Omega \boldsymbol{u}^T \boldsymbol{b} d\Omega + \int_{\Gamma_t} \boldsymbol{u}^T \bar{\boldsymbol{t}} d\Gamma \right) dt = 0 \tag{3.20}$$

Since all operators are linear, the variation operator can be moved inside the integrals,

$$\int_{t_1}^{t_2} \left(-\frac{1}{2}\int_\Omega \delta\left(\boldsymbol{\varepsilon}^T \boldsymbol{\sigma}\right) d\Omega + \int_\Omega \delta\left(\boldsymbol{u}^T \boldsymbol{b}\right) d\Omega + \int_{\Gamma_t} \delta\left(\boldsymbol{u}^T \bar{\boldsymbol{t}}\right) d\Gamma \right) dt = 0 \tag{3.21}$$

The first term of the previous equation can be developed. The integrand function can be written as,

$$\delta\left(\boldsymbol{\varepsilon}^T \boldsymbol{\sigma}\right) = \delta\boldsymbol{\varepsilon}^T \boldsymbol{\sigma} + \boldsymbol{\varepsilon}^T \delta\boldsymbol{\sigma} \tag{3.22}$$

These two terms are scalars. Therefore, the transpose does not affect the result. Having into account the constitutive equation $\boldsymbol{\sigma} = \boldsymbol{c}\boldsymbol{\varepsilon}$, and the symmetric property $\boldsymbol{c}^T = \boldsymbol{c}$, it is possible to write,

$$\boldsymbol{\varepsilon}^T \delta\boldsymbol{\sigma} = \delta\boldsymbol{\sigma}^T \boldsymbol{\varepsilon} = \delta\boldsymbol{\varepsilon}^T \boldsymbol{\sigma} \tag{3.23}$$

Therefore, equation 3.22 becomes,

$$\delta\left(\boldsymbol{\varepsilon}^T \boldsymbol{\sigma}\right) = 2\delta\boldsymbol{\varepsilon}^T \boldsymbol{\sigma} \tag{3.24}$$

and equation 3.21 can be rewritten as,

$$\int_{t_1}^{t_2} \left(-\int_\Omega \delta\left(\boldsymbol{\varepsilon}^T \boldsymbol{\sigma}\right) d\Omega + \int_\Omega \delta\left(\boldsymbol{u}^T \boldsymbol{b}\right) d\Omega + \int_{\Gamma_t} \delta\left(\boldsymbol{u}^T \bar{\boldsymbol{t}}\right) d\Gamma \right) dt = 0 \tag{3.25}$$

In order to satisfy equation 3.25 with all possible displacement fields $\boldsymbol{u}$, the integrand of the time integration must be null,

$$-\int_{\Omega}\delta\left(\boldsymbol{\varepsilon}^{T}\boldsymbol{\sigma}\right)d\Omega+\int_{\Omega}\delta\left(\boldsymbol{u}^{T}\boldsymbol{b}\right)d\Omega+\int_{\Gamma_{t}}\delta\left(\boldsymbol{u}^{T}\bar{\boldsymbol{t}}\right)d\Gamma=0 \tag{3.26}$$

This equation is known as the Galerkin weak form, which can also be viewed as the principal of virtual work.

Replacing equations 3.7 and 3.8 in equation 3.26, the generic Galerkin weak form can be obtained, written in terms of displacement,

$$-\int_{\Omega}\delta\left(\left(\boldsymbol{L}\boldsymbol{u}\right)^{T}\boldsymbol{c}\left(\boldsymbol{L}\boldsymbol{u}\right)\right)d\Omega+\int_{\Omega}\delta\left(\boldsymbol{u}^{T}\boldsymbol{b}\right)d\Omega+\int_{\Gamma_{t}}\delta\left(\boldsymbol{u}^{T}\bar{\boldsymbol{t}}\right)d\Gamma=0 \tag{3.27}$$

3.3 Discrete System Equations

The discrete system of equations for the RPIM is obtained through the the virtual work principle by using the RPIM interpolator functions for the trial and test functions. The domain Ω is discretized in a nodal mesh, and the nodal connectivity is imposed by the influence domain of each node. The RPIM trial function $\boldsymbol{u}\left(\boldsymbol{x}_{I}\right)$ is given by,

$$\boldsymbol{u}\left(\boldsymbol{x}_{I}\right)=\sum_{i=1}^{n}\varphi_{i}\left(\boldsymbol{x}_{I}\right)u_{i} \tag{3.28}$$

where $\varphi_{i}\left(\boldsymbol{x}_{I}\right)$ is the RPIM C^{∞} interpolator function and u_{i} is the displacement of each node inside the influence domain of the interest node $\boldsymbol{x}_{I}$.

The interpolation function satisfies the condition,

$$\varphi_{i}\left(\boldsymbol{x}_{j}\right)=\delta_{ij} \tag{3.29}$$

where δ_{ij} is the delta Kronecker,

$$\delta_{ij}=\begin{cases}1\,,i=j\\0\,,i\neq j\end{cases} \tag{3.30}$$

The test function is defined as,

$$d\boldsymbol{u}\left(\boldsymbol{x}_{I}\right)=\sum_{i=1}^{n}\varphi_{i}\left(\boldsymbol{x}_{I}\right)du_{i} \tag{3.31}$$

Using the virtual work equation, the stiffness matrix can be defined as,

$$\boldsymbol{K}=\int_{\Omega}\boldsymbol{B}^{T}\boldsymbol{c}\boldsymbol{B}d\Omega \tag{3.32}$$

where $\boldsymbol{B}$ is the deformability matrix,

$$\boldsymbol{B}^T = \begin{bmatrix} \dfrac{\partial \varphi_I}{\partial x} & 0 \\ 0 & \dfrac{\partial \varphi_I}{\partial y} \\ \dfrac{\partial \varphi_I}{\partial y} & \dfrac{\partial \varphi_I}{\partial x} \end{bmatrix} \tag{3.33}$$

The total force vector, which contains the body forces and the external forces, can be expressed by,

$$\boldsymbol{F} = \boldsymbol{f}_b + \boldsymbol{f}_{\bar{t}} = \int_\Omega \boldsymbol{H}^T \boldsymbol{b} d\Omega + \int_{\Gamma_t} \boldsymbol{H}^T \bar{\boldsymbol{t}} d\Gamma \tag{3.34}$$

where $\boldsymbol{H}$ is the interpolation function matrix defined as,

$$\boldsymbol{H} = \varphi \boldsymbol{I} \tag{3.35}$$

Therefore, equation 3.26 can be expressed in a condensed form,

$$-\delta \boldsymbol{U}^T [\boldsymbol{K}\boldsymbol{U} - \boldsymbol{F}] = 0 \tag{3.36}$$

Since the previous equation is valid for any virtual displacement, the linear system of equations is obtained,

$$\boldsymbol{K}\boldsymbol{U} = \boldsymbol{F} \tag{3.37}$$

3.3.1 Imposition of the Boundary Conditions

As mentioned previously, the interpolation functions possess the delta Kronecker property. Therefore, the boundary conditions, whether essential (related to displacements), or natural (related to forces applied) can be directly applied in the stiffness matrix.

3.4 Elastoplasticity

In the past, and due to the loading and service conditions of structures in general, only linear behaviour was considered in the designing process of said structures. However, many design offices today understand the advantages of the non-linear analysis, both economical and regarding safety. The elastoplasticity is one of the non-linear effects that can make the increasingly slender structural elements collapse [27].

The theory of plasticity has the main objective of defining the relations between stresses and strains for materials which exhibit an elastoplastic behaviour. These materials present an elastic behaviour until a certain stress level, called the yield stress, is achieved. Until this point, if the

material is unloaded, all the deformation is recovered. If the stress level goes beyond the yield stress, the material has a plastic behaviour, with irreversible deformations.

Different models can be used to described different elastoplastic behaviours. In the present work, the bilinear elastoplastic model is used, represented in figure 3.3

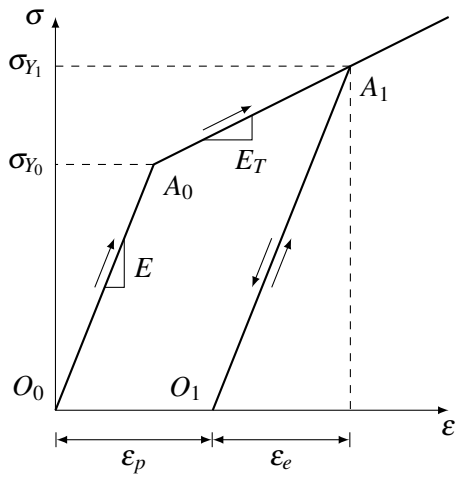

Figure 3.3: Bilinear Elastoplastic Model

In this model, after the yield stress is achieved, the material will start to exhibit plastic behaviour, and the relation between stress and strain is given by a tangent modulus E_T. It is visible that, after unloading, the elastic deformation was recovered, while the plastic deformation was not.

To fully describe the elastoplastic material behaviour, three fundamental concepts must be defined, in addition to the stress-strain relation [38]:

- **Yield criterion:** defines a region (yield surface) that limits the elastic behaviour of the material;
- **Flow rule:** defines the stress-strain relation in the plastic regime;
- **Hardening rule:** defines the evolution of the yield function with the plastic deformation.

Plastic behaviour is observable when there are irreversible strains on the solid after the load is removed. Since this behaviour is normally associated with constant volume deformations, the additive decomposition of strain rule can be used to defined the total strain vector, as,

$$\varepsilon = \varepsilon_e + \varepsilon_p \tag{3.38}$$

where ε_e represents the elastic component of strain and ε_p the plastic one.

Before the material enters the plastic state, Hooke's law (equation 3.8) defines the relation between stress and strain. However, after the material exceeds the stress level imposed by the yield criterion, Hooke's law is no longer valid, and the stress state evolves by the plastic flow rule [39].

3.5 Yield Criterion

The yield criterion mathematically defines the stress values that match the elastic limit behaviour of the material [40]. It is a function of the stress state and the loading history, and can be generally expressed by,

$$F(\boldsymbol{\sigma}, \boldsymbol{\varepsilon}_p, \kappa) = f(\boldsymbol{\sigma}, \boldsymbol{\varepsilon}_p, \kappa) - \sigma_Y(\kappa) = 0 \tag{3.39}$$

where $f(\boldsymbol{\sigma}, \boldsymbol{\varepsilon}_p, \kappa)$ is the yield function, dependent on the stress state $\boldsymbol{\varepsilon}_p$, the plastic strain $\boldsymbol{\varepsilon}_p$ and a hardening parameter κ. The stress $\sigma_Y(\kappa)$ represents the yield stress of the material.

Equation 3.39 can be simplified in the case of an isotropic material with an yield stress independent of κ [41],

$$F(\boldsymbol{\sigma}) = f(\boldsymbol{\sigma}) - \sigma_Y = 0 \tag{3.40}$$

In this work, Von Mises yield criterion is used, which is commonly applied to metals. Figure 3.4 shows a representation of the Von Mises and Tresca yield criteria in the Westergaard space. It is visible that the Tresca yield criterion presents edges in the surface, which are hard to deal with in terms of computation (due to discontinuities and singularities). The Von Mises criterion has a smooth surface, therefore the computation is easier when compared with the Tresca criterion.

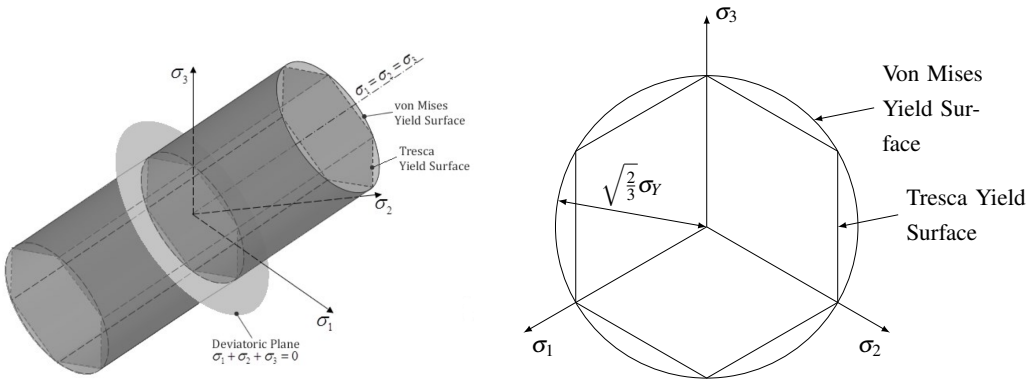

(a) (b)

Figure 3.4: Von Mises and Tresca Yield Criterion: (a) General View [31]; (b) Deviatoric Plane.

Von Mises suggested that the yielding occured when the second deviatoric stress invariant (I_2) reached a critical value [42], defined as,

$$I_2 = \frac{\sigma_Y}{\sqrt{3}} \tag{3.41}$$

The previous equation defines the surface of a cilinder circumscribed in the Tresca hexagon, and whose interception with the π plane is the circle represented on figure 3.4(b).

The Von Mises criterion can also be expressed as a function of the effective stress $\bar{\sigma}$,

$$\bar{\sigma}^2 = \sigma_Y^2 = 3I_2 \tag{3.42}$$

The second deviatoric stress invariant I_2 can be defined in terms of the cartesian components of stress,

$$\bar{\sigma} = \sqrt{\frac{1}{2}\left[(\sigma_{xx}-\sigma_{yy})^2+(\sigma_{yy}-\sigma_{zz})^2+(\sigma_{zz}-\sigma_{xx})^2+6\left(\sigma_{yz}^2+\sigma_{zx}^2+\sigma_{xy}^2\right)\right]} \tag{3.43}$$

Substituing the previous equation in equation 3.40, the following equation is obtained,

$$F(\sigma) = \sqrt{\frac{1}{2}\left[(\sigma_{xx}-\sigma_{yy})^2+(\sigma_{yy}-\sigma_{zz})^2+(\sigma_{zz}-\sigma_{xx})^2+6\left(\sigma_{yz}^2+\sigma_{zx}^2+\sigma_{xy}^2\right)\right]} - \sigma_Y = 0 \tag{3.44}$$

The yield function can be defined by many different expressions, each one having a distinct geometrical representation in the Westergaard space. The material to be simulated has to be taken into account when deciding the yield function to use [43].

3.6 Plastic Flow

By observing equation 3.40, it is possible to conclude that if $f < \sigma_Y$, the material is in the elastic domain, and $f = \sigma_Y$ represents the limit of the elastic domain and start of the plastic behaviour. Once this point is reached, the subsequent behaviour of the material is conditioned by the value of the variation of the yield function f with the stress $\boldsymbol{\sigma}$. This variation can be defined as,

$$df = \left(\frac{\partial f}{\partial \boldsymbol{\sigma}}\right)^T d\boldsymbol{\sigma} \tag{3.45}$$

where $\partial f/\partial \boldsymbol{\sigma}$ is the gradient of f, and consequently an orthogonal vector to the yield surface for a given stress $\boldsymbol{\sigma}$, as shown in figure 3.5.

The outcome of equation 3.45 can be divided into three situations. If $df < 0$, the stress point is inside the yield surface, and elastic unloading has occured. The relation between stress and strain is linear. If $df = 0$, the stress point is on the yield surface. This can represent a perfectly plastic state, in case the material has no hardening parameter κ, or otherwise the start of the plastification state. Finally, $df > 0$ corresponds to the plastic loading state, with the stress remaining in an expanding yield surface. At this point, the material is in a plastic flow state [41].

Introducing the concept of the plastic potential function, $g(\boldsymbol{\sigma}, \boldsymbol{\varepsilon}^p, \kappa)$, the flow rule can be defined as,

$$d\boldsymbol{\varepsilon}_p = d\lambda \frac{\partial g}{\partial \boldsymbol{\sigma}} \tag{3.46}$$

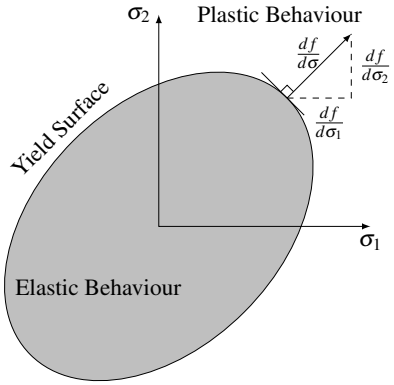

Figure 3.5: Orthogonality Condition in a Two-Dimensional Stress Space

where $d\lambda$ is the plastic strain-rate multiplier [43]. The plastic multiplier defines the magnitude of the plastic strain increment vector, while the gradient of the plastic potential defines the direction. In this work, an associative flow rule is used. This means that the plastic potential function is actually the yield function $f(\boldsymbol{\sigma}, \boldsymbol{\varepsilon}^p, \kappa)$, and so equation 3.46 can be rewritten as,

$$d\boldsymbol{\varepsilon}_p = d\lambda \frac{\partial f}{\partial \boldsymbol{\sigma}} \tag{3.47}$$

As mentioned earlier, the vector $\frac{\partial f}{\partial \boldsymbol{\sigma}}$ is normal to the yield surface. Therefore the plastic strain increment vector is also normal to the yield surface. This orthogonality ensures a unique solution [39].

3.7 Hardening Rule

The hardening rule has the objective of describing the conditions for a new plastic flow, given that the plastic phase of the material has been achieved. These conditions are essential, since the yield surface may change its size and shape with the increasing plastic deformation. Two types of hardening rules may be defined, depending on how the hardening parameter κ is calculated. These are strain hardening and work hardening.

Figure 3.6 presents some strain hardening models.

A perfect plastic material has no hardening parameter κ and its yield surface never changes size or shape.

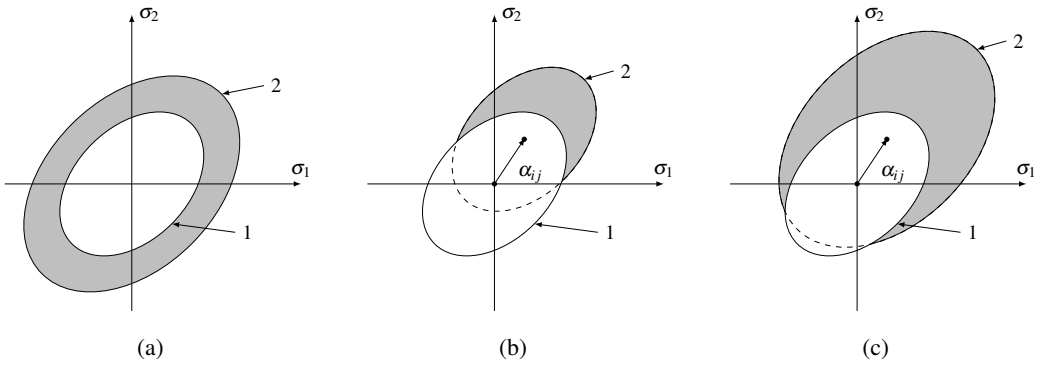

Figure 3.6: Hardening Rules: (a) Isotropic Hardening; (b) Kinematic Hardening; (c) Mixed Hardening.

In the isotropic hardening rule, figure3.6(a), it is assumed that the yield surface expands uniformly without distortion or movement.

Figure 3.6(b) represents the Kinematic Hardening Rule. In this case, the yield surface evolves by moving in relation to its initial origin, without changing its size.

With the different types of movements (expansion, translation and even rotation), many hardening models can be defined [39], as is the example of the mixed hardening rule, represented in figure 3.6(c).

Generically, the yield criterion can be written as,

$$F(\boldsymbol{\sigma}, \boldsymbol{\varepsilon}_p, \boldsymbol{\alpha}, \kappa) = f(\boldsymbol{\sigma}, \boldsymbol{\varepsilon}_p, \boldsymbol{\alpha}, \kappa) - k^2(\kappa) = 0 \tag{3.48}$$

being k^2 the yield surface size, $f(\boldsymbol{\sigma}, \boldsymbol{\varepsilon}_p, \boldsymbol{\alpha}, \kappa)$ the yield surface shape and $\boldsymbol{\alpha}$ the centre of the yield surface.

In this work, the isotropic hardening rule is used. Therefore, equation 3.48 can be simplified,

$$f(\boldsymbol{\sigma}) = k^2(\kappa) \tag{3.49}$$

By applying the Von Mises criterion, the previous equation becomes,

$$F(\boldsymbol{\sigma}, k) = 3I_2 - \sigma_Y^2(\kappa) \tag{3.50}$$

The hardening parameter κ can be obtained by the effective plastic strain $\bar{\varepsilon}_p$,

$$\bar{\varepsilon}_p = \int d\bar{\varepsilon}_p = \int \sqrt{\frac{2}{3} d\boldsymbol{\varepsilon}_p d\boldsymbol{\varepsilon}_p} \tag{3.51}$$

Therefore, the κ parameter is simply defined as,

$$\kappa = \bar{\varepsilon}_p \tag{3.52}$$

Chapter 4

Nonlinear Solution Algorithms

The elastoplastic analysis of structures requires the solution of a set of non linear equations. These equations can't be solved by direct methods. Therefore, two types of numerical algorithms can be employed to obtain a solution, the incremental method and the incremental and iterative method, also know as the Newton-Rapson method. The incremental algorithm is very simple and intuitive. The non linear problem is simplified to a series of linear solutions, where the loads are applied incrementally until the desire value is reached. However, the method usually has a bad performance for considerable non linearities, leading to great errors [42].

The Newton-Rapson method overcomes the problems of the previous method, since in every load increment, there is an iteration process that reduces the transition error between load increments to an insignificant value.

Figure 4.1(a) represents the incremental and iterative Newton-Rapson method. Even though this method generates very good results in relation to the convergence to the final solution, this method is a very slow numerical procedure, since the stiffness matrix and its inverse must be recalculated in every iteration process.

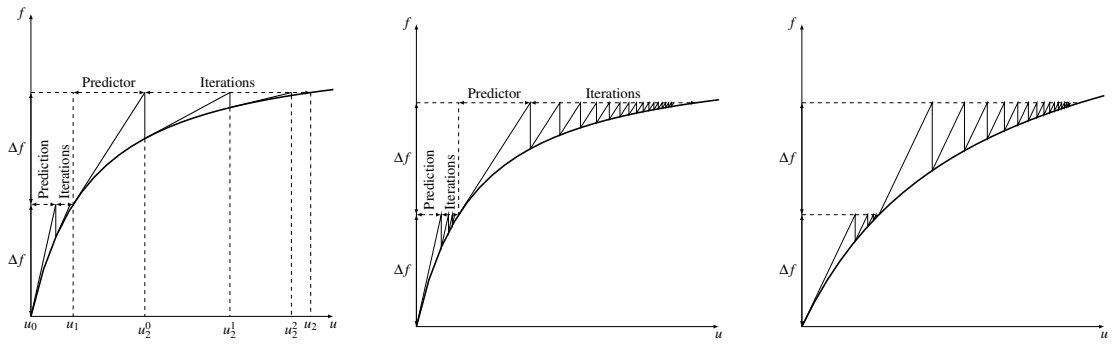

(a) (b) (c)

Figure 4.1: Newton-Rapson Methods: (a) Classic Newton-Rapson; (b) Initial Increment Stiffness Variation (KT1); (c) Initial Stiffness Variation (KT0).

In order to reduce the computational cost, several modified versions of the Newton-Rapson were developed.

The first variant is the initial increment stiffness method (KT1), represented in figure 4.1(b). In this variation, the stiffness matrix is calculated at the start of each load increment, and remains constant throughout the entire iteration process. This results in a lower computational cost, however it has slower convergence.

Further simplifications can be made to the KT1 method. Figure 4.1(c) represents the initial stiffness method, in which the stiffness matrix is only calculated in the first increment and used throughout the whole process. When compared with the KT1 method, the KT0 has lower computational cost, since there is only one calculation and inversion of the stiffness matrix. However, more iterations are required to achieve the value of the incremental load.

4.1 KT0 Algorithm

As mentioned previously, the KT0 algorithm is used in this work, which is described in this section. The main characteristic of this method is the single calculation of the stiffness matrix and its inverse at the start of the first load increment.

Before the KT0 is ready to initiate, initial data must be introduced, such as: problem dimensions and discretization information, material properties, maximum load, essencial boundary conditions and the number of increments and iterations of the algorithm.

With this information, the nodal mesh is constructed, along with the integration mesh. The influence domains are defined and the interpolation functions are calculated. With the material properties and the nodal connectivity, the initial stiffness matrix can be determined. With the natural and essential boundary conditions, the final stiffness matrix $\boldsymbol{K}_0$ is obtained. After this pre-processing phase, the KT0 algorithm can start.

The incremental load $\boldsymbol{f}_i$ is defined as,

$$\boldsymbol{f}_i = \frac{\boldsymbol{F}}{inc} \tag{4.1}$$

where $\boldsymbol{F}$ is the maximum load and inc is the number of increments.

The displacement field can be obtained by,

$$\boldsymbol{u}_i = \boldsymbol{K}_0^{-1} \boldsymbol{f}_i \tag{4.2}$$

and consequently the stress field,

$$\boldsymbol{\sigma}_i = \boldsymbol{c}\boldsymbol{B}\boldsymbol{u}_i \tag{4.3}$$

The stress state is verified for every Gauss point. If the stress passes the yield surface, the return algorithm is applied. In the end of this process, the actualized stress vector of the increment, Δ

$$\boldsymbol{\sigma}_i = \boldsymbol{\sigma}_{i-1} + \Delta\boldsymbol{\sigma} \tag{4.4}$$

where $\boldsymbol{\sigma}_{i-1}$ is the total stress vector of the previous increment.

If any Gauss point passed the yield surface in the present increment or iteration, the residual forces must be calculated, using the following equation,

$$\boldsymbol{f}_i^{res} = \boldsymbol{f}_i - \int_{\Omega} \boldsymbol{B}^T \Delta\boldsymbol{\sigma} d\Omega \tag{4.5}$$

The value of the residual forces is zero if no Gauss point passed the yield surface.

In order to check whether the residual forces are significant or not, the following equation is calculated,

$$\frac{\left(\frac{\sum_{m=1}^{n} \boldsymbol{f}_i^{res}{}_m}{n} \right)}{\sum_{k=1}^{j} \left(\frac{\sum_{m=1}^{n} \boldsymbol{f}_i^{res}{}_m}{n} \right)} < toler \tag{4.6}$$

where n is the number of nodes and j is the number of iterations.

This serves as a stop criterion, where $toler$ is the value introduced to define how significant the residual forces can be.

If the equation is verified, the algorithm goes to the next load increment. Otherwise, the residual forces are still too big, and they must be applied to the structure. To do this, the process described in this section is repeated, replacing the incremental force defined in equation 4.1 for the residual force.

When all the load increments are applied, the algorithm stops, and the load-displacement curves, as well as the stress and displacement fields can be obtained.

4.2 Mathematical Plasticity

Since this work as the objective of analysing elastoplastic problems, it makes sense to present the concepts shown in chapter 3 in a matricial form [42].

The elastic strain vector can be defined using Hooke's law,

$$d\boldsymbol{\varepsilon} = \boldsymbol{c}^{-1} d\boldsymbol{\sigma} \tag{4.7}$$

Once the material elastic limit is achieved, the previous equation is no longer valid, since the total deformation now has a plastic and irreversible component.

4.2.1 Uniaxial Yielding

Considering an uniaxial test for a elastoplastic material, which generates the stress/strain curve presented in figure 3.3. It is visible that the material has an elastic behaviour, characterized by the elastic modulus, until the yield stress is achieved. After this point, the stress/strain relation is given by the tangent modulus.

Having into account figure 3.3, the hardening parameter H' can be defined by,

$$H'(\boldsymbol{\varepsilon}_p) = \frac{\partial \bar{\boldsymbol{\sigma}}}{\partial \bar{\boldsymbol{\varepsilon}}_p} = \frac{d\boldsymbol{\sigma}}{d\boldsymbol{\varepsilon} - d\boldsymbol{\varepsilon}_e} = \frac{1}{\frac{d\boldsymbol{\varepsilon}}{d\boldsymbol{\sigma}} - \frac{d\boldsymbol{\varepsilon}_e}{d\boldsymbol{\sigma}}} = \frac{1}{\frac{1}{E_T} - \frac{1}{E}} = \frac{E_T}{1 - \frac{E_T}{E}} \tag{4.8}$$

Therefore, H' can be determined by a simple uniaxial test.

4.2.2 Plastic Flow Rule

The expression of the Von Mises yield criterion is again presented,

$$F(\boldsymbol{\sigma}, \boldsymbol{\varepsilon}_p, \kappa) = f(\boldsymbol{\sigma}, \boldsymbol{\varepsilon}_p, \kappa) - \sigma_Y(\kappa) = 0 \tag{4.9}$$

Differentiating the previous equation, the following equation is obtained,

$$dF = \left(\frac{\partial f}{\partial \boldsymbol{\sigma}}\right)^T d\boldsymbol{\sigma} - \frac{\partial \sigma_Y}{\partial \kappa} d\kappa = 0 \tag{4.10}$$

which can be also expressed as,

$$dF = \boldsymbol{a}^T d\boldsymbol{\sigma} - A d\lambda = 0 \tag{4.11}$$

where $\boldsymbol{a}$ is the flow vector, normal to the yield surface, $d\lambda$ is the plastic strain-rate multiplier and A is defined as,

$$A = \frac{1}{d\lambda} \frac{\partial \sigma_Y}{\partial \kappa} d\kappa \tag{4.12}$$

The relation between stress and strain variation can be expressed by,

$$d\boldsymbol{\sigma} = \boldsymbol{c} \cdot d\boldsymbol{\varepsilon}_e = \boldsymbol{c} \cdot d\boldsymbol{\varepsilon} - d\lambda \cdot \boldsymbol{c} \cdot \boldsymbol{a} \tag{4.13}$$

The plastic strain-rate multiplier $d\lambda$ can be defined by applying equation 4.13 to equation 4.11,

$$d\lambda = \frac{\boldsymbol{a}^T \boldsymbol{c} d\boldsymbol{\varepsilon}}{\boldsymbol{a}^T \boldsymbol{c} \boldsymbol{a} + A} \tag{4.14}$$

The plastic deformation can now be obtained by,

$$\boldsymbol{\varepsilon_p} = d\lambda \boldsymbol{a} \tag{4.15}$$

Strain hardening is used in this work, and by applying equation 3.52,

$$d\kappa = d\bar{\varepsilon}_p = \sqrt{\frac{2}{3} d\boldsymbol{\varepsilon}_p^T d\boldsymbol{\varepsilon}_p} \tag{4.16}$$

Taking into account equation 3.47 and the definition of the flow vector $\boldsymbol{a} = \frac{\partial f}{\partial \boldsymbol{\sigma}}$, the previous equation becomes,

$$d\kappa = d\lambda \sqrt{\frac{2}{3} \boldsymbol{a}^T \boldsymbol{a}} \tag{4.17}$$

The A parameter can be obtained from equation 4.12,

$$A = \frac{\sigma_Y}{dk} \sqrt{\frac{2}{3} \boldsymbol{a}^T \boldsymbol{a}} = \frac{\sigma_Y}{dk} \bar{a} \tag{4.18}$$

A linear variation is considered for the yield stress,

$$\sigma_Y \left(\kappa = \bar{\boldsymbol{\varepsilon}}_p \right) = \sigma_Y^0 + H' \bar{\boldsymbol{\varepsilon}}_p \tag{4.19}$$

Therefore, the parameter A becomes,

$$A = H' \bar{a} \tag{4.20}$$

When the Von Mises criterion is used, $\bar{a} = 1$, and so,

$$A = H' \tag{4.21}$$

4.2.3 Stress/Strain Relation

As mentioned previously, Hooke's law is not valid once the plastic phase is achieved. Hence, the stress variation can be expressed as a function of the strain variation by substituting equation 4.14 in equation 4.13,

$$d\boldsymbol{\sigma} = \boldsymbol{c}_{ep} d\boldsymbol{\varepsilon} \tag{4.22}$$

where $\boldsymbol{c}_{ep}$ is defined by,

$$c_{ep} = \boldsymbol{c} - \frac{\boldsymbol{c}\boldsymbol{a}\boldsymbol{a}^T \boldsymbol{c}}{A + \boldsymbol{a}^T \boldsymbol{c}\boldsymbol{a}} \tag{4.23}$$

Defining $\boldsymbol{d}_D = \boldsymbol{c}\boldsymbol{a}$, the previous equation becomes,

$$\boldsymbol{c}_{ep} = \boldsymbol{c} - \frac{\boldsymbol{d}_D \boldsymbol{d}_D^T}{A + \boldsymbol{d}_D^T \boldsymbol{a}} \tag{4.24}$$

4.2.4 Stress Return Algorithm

After a new load increment, stresses might go out of the yield surface, which is physically incorrect. Therefore, an algorithm is necessary to ensure the stresses remain within the yield surface. Many algorithms can be used to achieve this goal [43], and in this work the forward-Euler scheme is used, represented in figure 4.2.

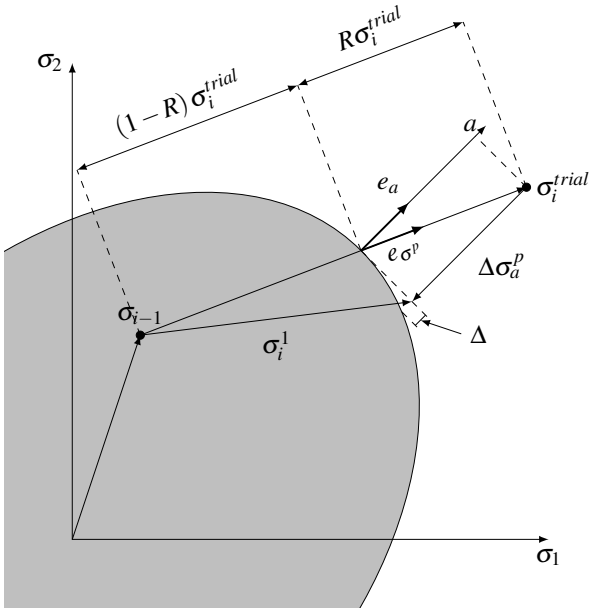

Figure 4.2: Forward-Euler Procedure

After a load increment, the trial stress σ_i^{trial} is obtained, which sits outside the actualized yield surface. The reduction factor R can be calculated by,

$$R = \frac{\bar{\sigma}_i^{trial} - \sigma_Y}{\bar{\sigma}_i^{trial} - \bar{\sigma}_{i-1}} \tag{4.25}$$

where $\bar{\sigma}$ represents the $\boldsymbol{\sigma}$ effective stress and σ_Y is the actualized yield stress. The reduction factor alows the trial stress to be divided in two parts, $(1-R)\,\sigma_i^{trial}$ inside and $R\sigma_i^{trial}$ outside the yield surface.

The flow vector $\boldsymbol{a}$ is calculated at the intersection point of the trial stress with the yield surface. As it is visible, the flow vector is normal to the yield surface.

The outside component of the trial stress, $R\sigma_i^{trial}$, is projected onto the flow vector, being the result $\Delta\sigma_a^p$. This vector is subtracted to the trial stress, returning the stress to the yield surface. However it is visible that, since the yield surface is curved, the new stress state is not yet on the yield surface. Therefore, this process is repeated untill $\Delta \cong 0$.

4.2.5 Implemented Algorithm

Figure 4.3 shows the algorithm implemented in this work. The input data such as the geometry, material properties, loading and boundary conditions allow the calculation of the stiffness matrix. A force increment can then be applied. After that, and for each integration point, the effective stress level is verified. If the stress is greater than the yield stress, the returning stress algorithm is applied. The next step consists of updating the stresses and calculating the residual forces. In order to check if the residual forces are too big, a tolerance is calculated, given by equation 4.6. If the tolerance is greater than a defined value, the residual forces are applied to the model. When the tolerance is small enough, the cycle ends, and a new load increment can be applied.

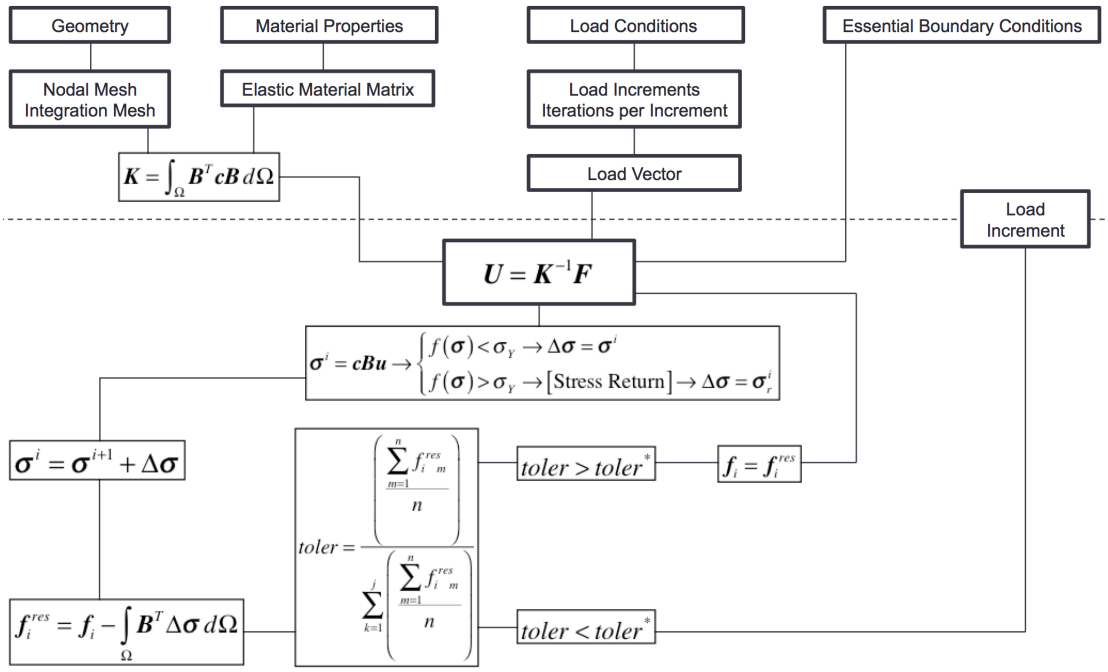

Figure 4.3: Implemented KT0 Algorithm

Chapter 5

Linear Applications

In this chapter, some linear elastic examples are analysed, in order to show the performance of the RPIM before the study of the elastoplastic examples in Chapter 6. The models studied are the square plate under parabolic stress, the cantilever beam and the square plate with a central hole [44].

5.1 Square Plate Under Parabolic Stress

The first example is a square plate subjected to a parabolic stress. Due to simmetry, only a quarter of the plate is analysed. The stress field is given by [44],

$$\begin{aligned}
\sigma_{xx} &= \sigma_0 \left(\frac{x^2}{L^2} - \frac{y^2}{D^2} \right) \\
\sigma_{yy} &= \sigma_0 \left(\frac{x^2 \left(L^2 - 2D^2 \right)}{L^2 \cdot D^2} + \frac{y^2}{L^2} \right) \\
\sigma_{xy} &= -\sigma_0 \left(\frac{2x.y}{L^2} \right)
\end{aligned} \tag{5.1}$$

The material, loading, geometry and boundary conditions are presented in figure 5.1(a). The model is discretized in both regular and irregular meshes. Figure 5.1(b) and figure 5.1(c) represent a regular and an irregular mesh of 289 nodes, which will be used in the analysis.

The analytical displacement solution for this problem is given by,

$$\begin{aligned}
u &= \frac{\sigma_0}{E} \left[\frac{x^3}{3L^2} - \frac{x \cdot y^2}{D^2} - \nu \left(\frac{x^3 \left(L^2 - 2D^2 \right)}{3L^2 \cdot D^2} + \frac{x.y^2}{L^2} \right) \right] \\
v &= \frac{\sigma_0}{E} \left[\frac{x^2.y \left(L^2 - 2D^2 \right)}{L^2.D^2} + \frac{y^3}{3L^2} - \nu \left(\frac{x^2.y}{L^2} - \frac{y^3}{3D^2} \right) \right]
\end{aligned} \tag{5.2}$$

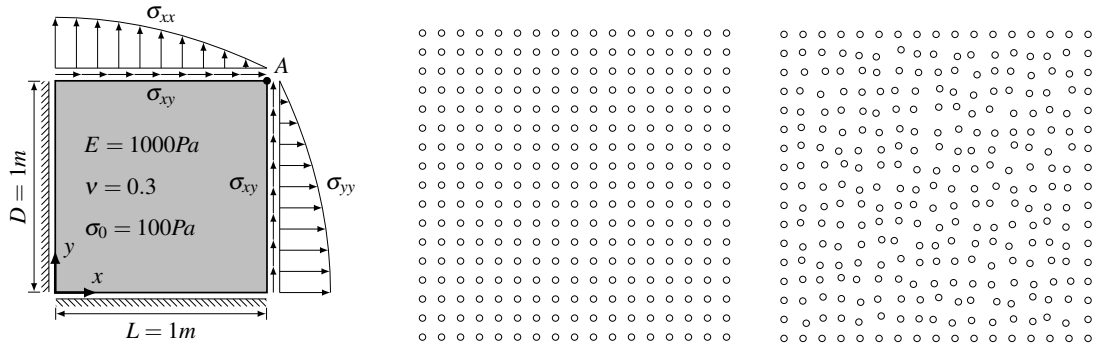

(a) (b) (c)

Figure 5.1: Square Plate Under Parabolic Stress: (a) Material and Geometric Conditions; (b) Regular 289 Node Mesh; (c) Irregular 289 Node Mesh.

The convergence study for the displacement values of point A (represented in figure 5.1(a)) is presented in figure 5.2.

It is possible to observe from figure 5.2 that the converged results are very close to the exact solution ($u_A = -0.0867$ and $v_A = -0.0867$) using both regular and irregular meshes.

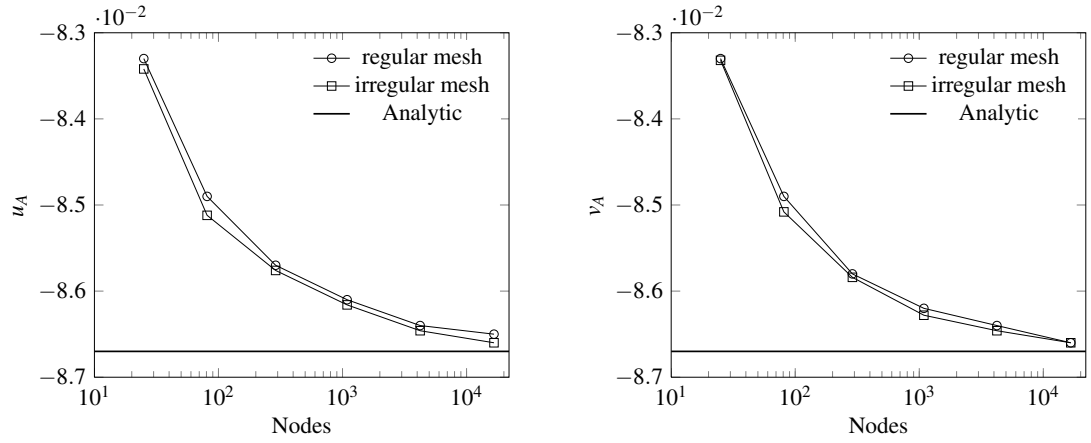

(a) (b)

Figure 5.2: Square Plate Under Parabolic Stress: (a) Displacement u_A; (b) Displacement v_A.

The results for the convergence study of the medium displacement error, equation 5.3 (where n is the number of nodes), are presented in figure 5.3(a). It is visible that the use of either regular or irregular meshes has no considerable impact on the error, and the converged error is very low (0.1%).

$$\Theta = \frac{1}{n}\sum_{i=1}^{n}\frac{\sqrt{(u_i - u_{i\,exact})^2 + (v_i - v_{i\,exact})^2}}{\sqrt{{u_{i\,exact}}^2 + {v_{i\,exact}}^2}} \tag{5.3}$$

The study made for the medium displacement error can also be made for the medium stress error. The problem should generate the stress field given by equation 5.1, therefore the medium stress error is calculated using the expression,

$$\Theta_{\sigma_k} = \frac{1}{n_Q} \sum_{i=1}^{n_Q} \frac{|\sigma_{k\,i} - \sigma_{k\,i\,exact}|}{|\sigma_{k\,i\,exact}|} \tag{5.4}$$

Where n_Q is the number of integration points, and σ_k represents the three stresses, σ_{xx}, σ_{yy} and σ_{xy}.

The results for the medium stress error, using regular meshes, are presented in figure 5.3(b). The converged error is low (below 3%), and the use of regular or irregular meshes has no effect on the medium error.

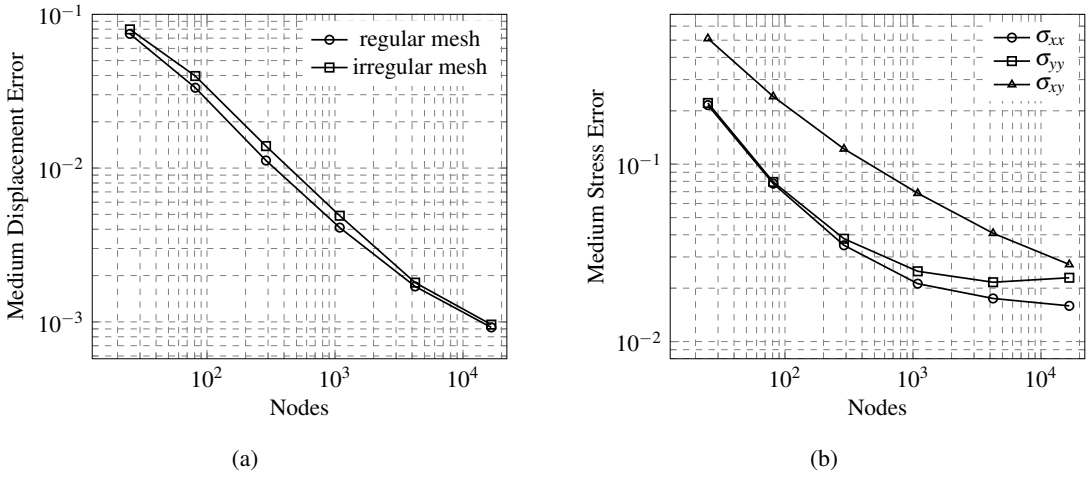

Figure 5.3: Square Plate Under Parabolic Stress: (a) Medium Displacement Error; (b) Medium Stress Error.

Another interesting analysis is the study of the obtained stress field. Figure 5.4 presents the stress distributions along interest lines of the solid, using a regular mesh of $129 \times 129 = 16641$ nodes.

In figure 5.4(a) it is possible to observe the evolution of the normal stress σ_{xx} along the line $x = 0$, whereas figure 5.4(b) presents the shear stress σ_{xy} distribution along the line $x = L/2$.

The results show that the RPIM solution for these stress distributions is almost indistinguishable from the analytical solution.

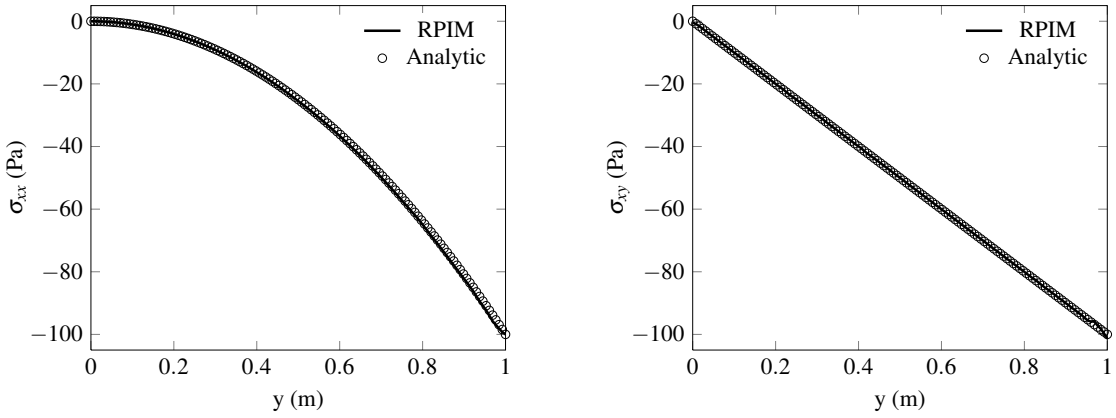

(a) (b)

Figure 5.4: Square Plate Under Parabolic Stress: (a) σ_{xx} Stress Along $x = 0$; (b) σ_{xy} Stress Along $x = L/2$.

The displacement field and stress field distributions for the complete domain are displayed in figure 5.1. Is is possible to observe that the variable fields produced are extremely smooth.

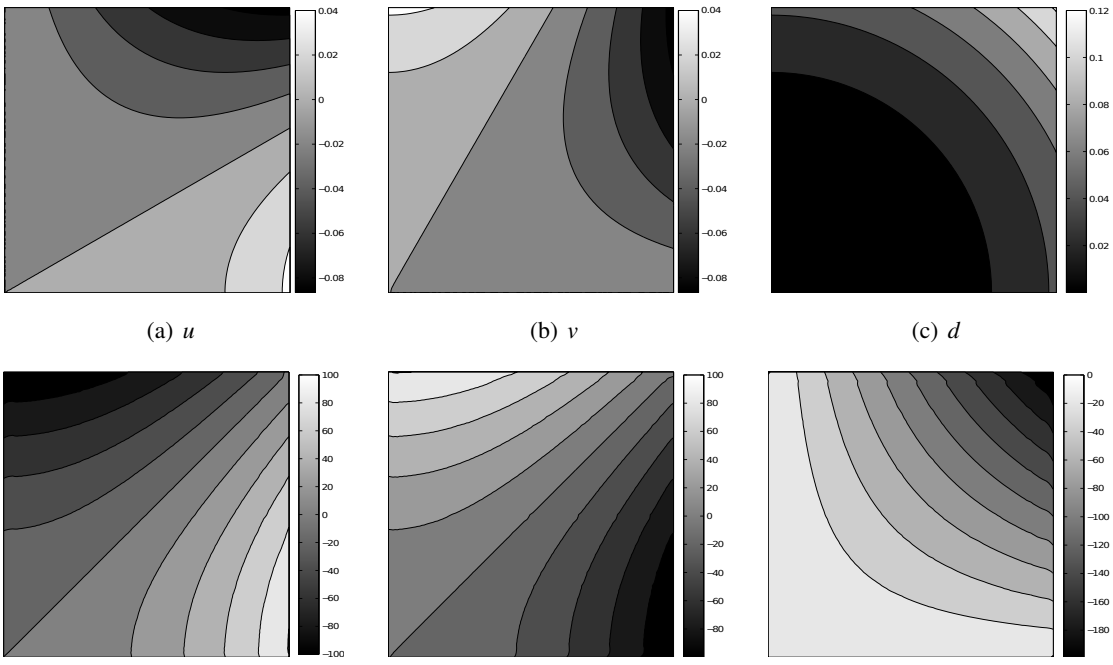

(a) u (b) v (c) d

(d) σ_{xx} (e) σ_{yy} (f) σ_{xy}

Square Plate Under Parabolic Stress: Displacement Field and Stress Field Distributions

5.2 Cantilever Beam

The second example is a cantilever beam, represented in Figure 5.6(a). The stress field applied is given by,

$$\sigma_{xx} = \sigma_0 \left(\frac{x^2}{L^2} - \frac{y^2}{D^2} \right)$$

$$\sigma_{yy} = \sigma_0 \left(\frac{x^2 \left(L^2 - 2D^2\right)}{L^2 \cdot D^2} + \frac{y^2}{L^2} \right) \tag{5.5}$$

$$\sigma_{xy} = -\sigma_0 \left(\frac{2x.y}{L^2} \right)$$

The geometry of the model, the boundary and loading conditions, as well as the mechanical properties are presented in figure 5.6(a). Both regular and irregular meshes were analysed. Figure 5.6(b) and figure 5.6(c) represent a regular and an irregular mesh of 561 nodes.

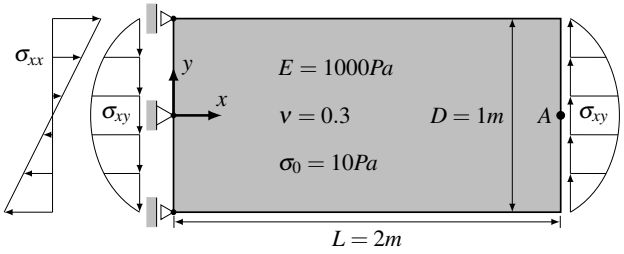

(a)

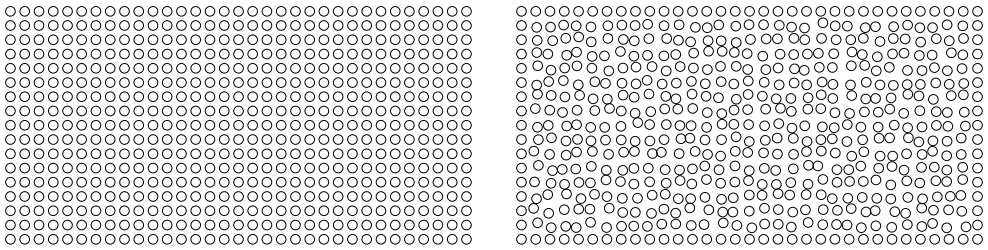

(b) (c)

Figure 5.6: Cantilever Beam: (a) Material and Geometric Conditions; (b) Regular 561 Node Mesh; (c) Irregular 561 Node Mesh.

The analytical displacement solution for this model is given by [44],

$$\begin{aligned} u &= \frac{\sigma_0}{E} \left[\frac{x^3}{3L^2} - \frac{x \cdot y^2}{D^2} - \nu \left(\frac{x^3 \left(L^2 - 2D^2\right)}{3L^2 \cdot D^2} + \frac{x.y^2}{L^2} \right) \right] \\ v &= \frac{\sigma_0}{E} \left[\frac{x^2.y \left(L^2 - 2D^2\right)}{L^2.D^2} + \frac{y^3}{3L^2} - \nu \left(\frac{x^2.y}{L^2} - \frac{y^3}{3D^2} \right) \right] \end{aligned} \tag{5.6}$$

Figure 5.7 shows the convergence study for the vertical displacement of point A (represented in figure 5.6(a)). The horizontal displacement is not presented, because the analytical solution is 0, and the erros obtained with RPIM are of the order of computer precision (10^{-15}).

It is possible to observe that the converged result for the vertical displacement is very close to the analytical solution ($v_A = 0.375$), whether regular or irregular meshes are used.

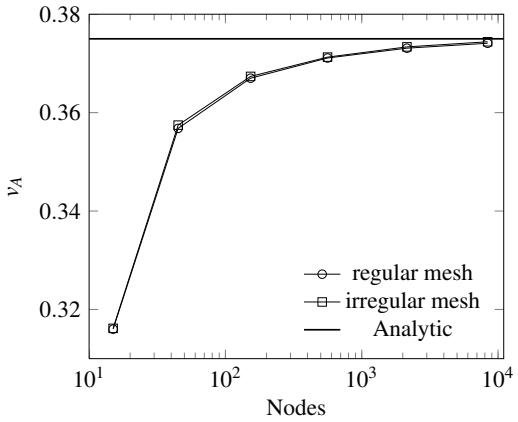

Figure 5.7: Cantilever Beam: v_A Displacement

Figure 5.8(a) shows the results for the convergence study of the medium displacement error. The medium error was calculated using the same equation 5.3 that was used for the first example. It is visible that the influence of the type of mesh in the medium displacement error is negligible, and the converged error is very low (0.5%).

The same logic was used to analyse the convergence of the medium stress error (equation 5.4). The results obtained with regular meshes are presented in figure 5.8(b). The converged medium stress error is low (5%), and the irregular meshes produce very similar results.

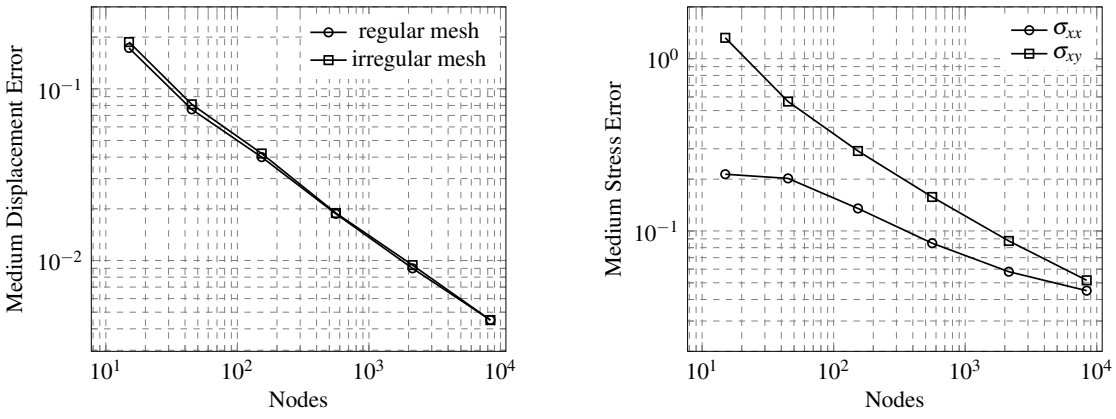

Figure 5.8: The Cantilever Beam: (a) Medium Displacement Error; (b) Medium Stress Error.

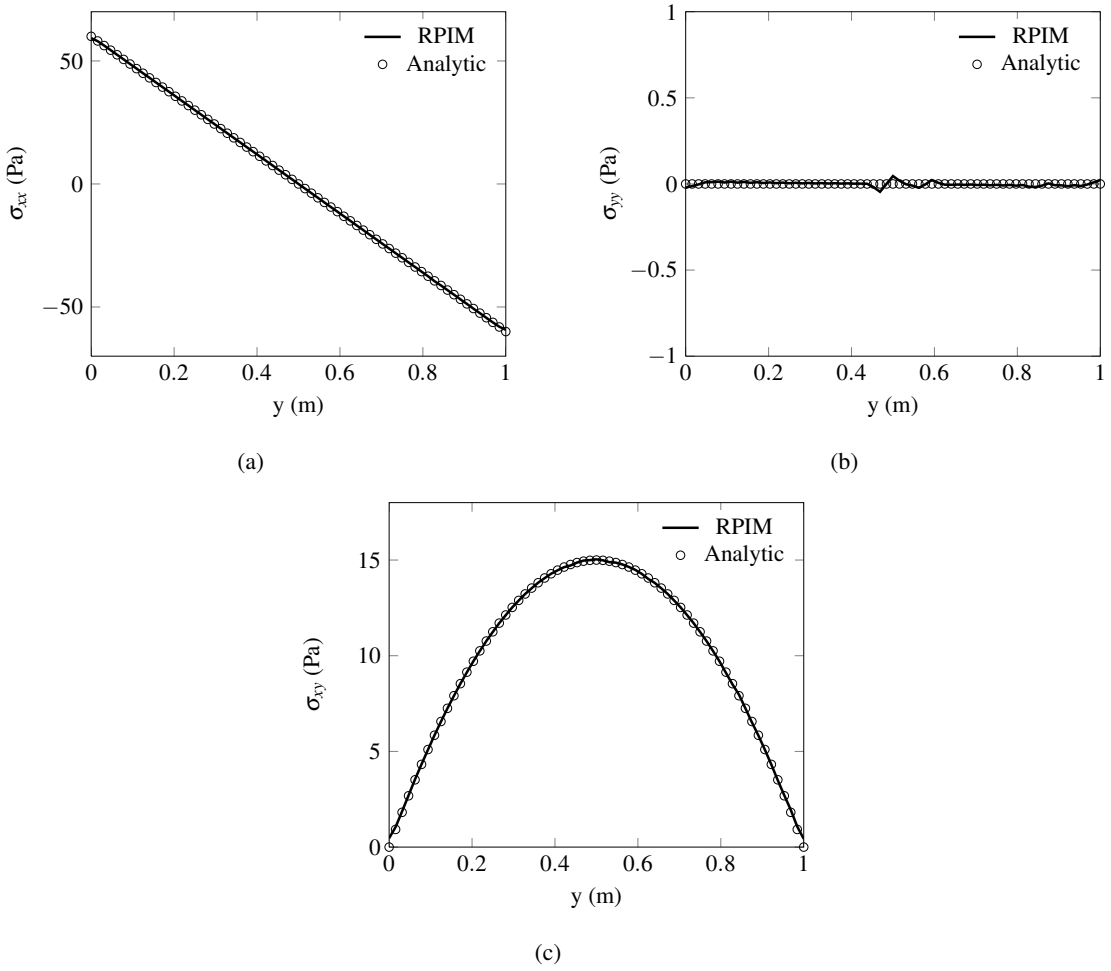

Figure 5.9: Cantilever Beam: (a) σ_{xx} Stress Along $x = L/2$; (b) σ_{yy} Stress Along $x = L/2$; (c) σ_{xy} Stress Along $x = L/2$.

Following the line of thought of the first example, the next analysis refers to the stress distribution along some interest lines of the solid. The following distributions were obtained using a regular mesh of $129 \times 65 = 8385$ nodes.

Figure 5.9 shows the evolutio of the three stresses (σ_{xx} in 5.9(a), σ_{yy} in 5.9(b) and σ_{xy} in 5.9(c)) along the line $x = L/2$.

Apart from a small oscillation in the σ_{yy} stress, the RPIM and the analytical solution are practically the same.

The displacement field and stress field distributions for the complete domain are displayed in figure 5.10. It is visible that the variable fields produced are very smooth.

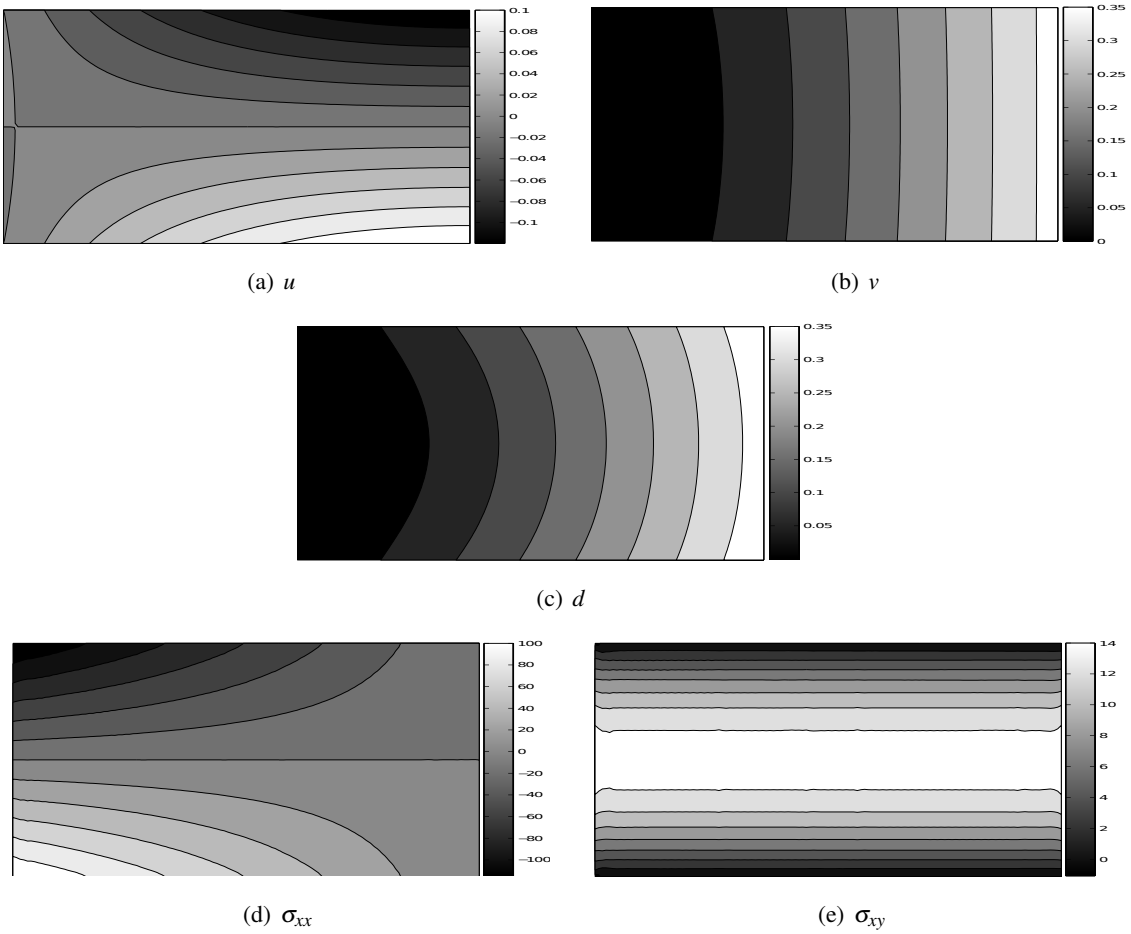

(a) u (b) v

(c) d

(d) σ_{xx} (e) σ_{xy}

Figure 5.10: Cantilever Beam: Displacement Field and Stress Field Distributions.

5.3 Square Plate with a Circular Hole

The final elastic example is a square plate with a circular hole. Figure 5.11(a) represents the simplified model analysed, since there are two planes of symmetry. The stress field applied is given by [44],

$$\begin{aligned}
\sigma_{xx} &= \sigma_0 \left[1 - \frac{a^2}{r^2} \left(\frac{3}{2}\cos(2\theta) + \cos(4\theta) \right) + \frac{3a^4}{2r^4}\cos(4\theta) \right] \\
\sigma_{yy} &= \sigma_0 \left[-\frac{a^2}{r^2} \left(\frac{1}{2}\cos(2\theta) - \cos(4\theta) \right) - \frac{3a^4}{2r^4}\cos(4\theta) \right] \\
\sigma_{xy} &= \sigma_0 \left[-\frac{a^2}{r^2} \left(\frac{1}{2}\sin(2\theta) + \sin(4\theta) \right) + \frac{3a^4}{2r^4}\sin(4\theta) \right]
\end{aligned} \tag{5.7}$$

The boundary conditions and the mechanical properties are presented in figure 5.11(a), while figures 5.11(b) and 5.11(c) represent a regular and an irregular mesh of 276 nodes each.

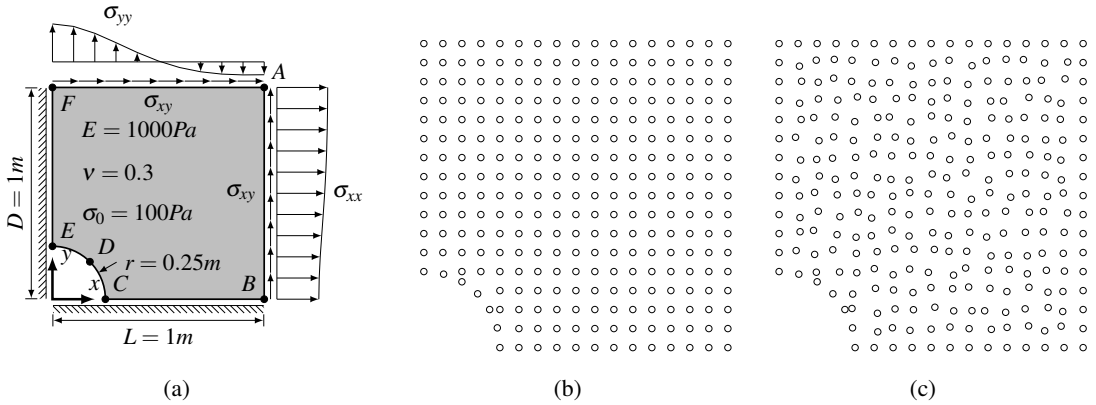

(a) (b) (c)

Figure 5.11: Square Plate with a Circular Hole: (a) Material and Geometric Conditions; (b) Regular 276 Node Mesh; (c) Irregular 276 Node Mesh.

The exact solution for the displacement is given by,

$$\begin{aligned} u &= \frac{\sigma_0 (1+\bar{\nu})}{\bar{E}} \left((1-\bar{\nu}) \left(r + \frac{2a^2}{r} \right) \cos\theta + \left(\frac{a^2}{2r} - \frac{a^4}{2r^3} \right) \cos(3\theta) \right) \\ v &= \frac{\sigma_0 (1+\bar{\nu})}{\bar{E}} \left(\left(-\bar{\nu} r - (1-2\bar{\nu}) \frac{a^2}{r} \right) \sin\theta + \left(\frac{a^2}{2r} - \frac{a^4}{2r^3} \right) \sin(3\theta) \right) \end{aligned} \tag{5.8}$$

where $\bar{\nu}$ and $\bar{E}$ are defined as,

$$\begin{aligned} \bar{\nu} &= \nu / (1+\nu) \\ \bar{E} &= E \left(1 - \bar{\nu}^2 \right) \end{aligned} \tag{5.9}$$

Figure 5.12 shows the convergence results for the displacement values of points A to F (represented in figure 5.11(a)).

By analysing figure 5.12, it is possible to observe that the converged results are close to the analytical solution, and in general, the type of mesh has low impact on the solution.

The convergence study for the medium displacement error is presented in figure 5.13(a). It is visible that the converged errors are very low, although the difference between the use of regular or irregular meshes is slightly bigger when compared to the previous examples.

Figure 5.13(b) shows the the results for the convergence study of the medium σ_{xx} stress error, using a regular mesh. The results for irregular meshes are similar to the ones presented, and the converged error is low (below 2%).

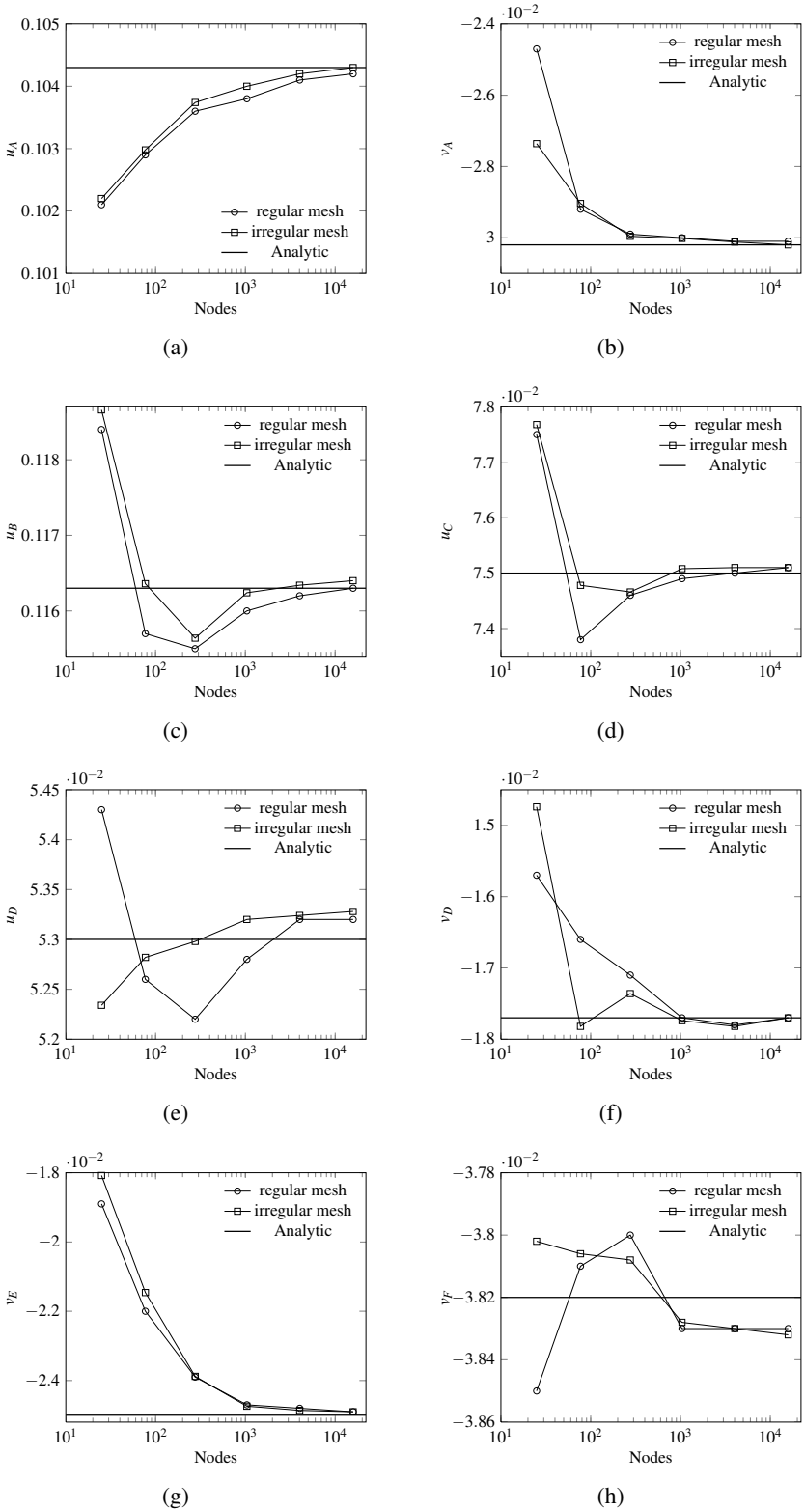

Figure 5.12: Square Plate with a Circular Hole: (a) u_A Displacement; (b) v_A Displacement; (c) u_B Displacement; (d) u_C Displacement; (e) u_D Displacement; (f) v_D Displacement; (g) v_E Displacement; (h) v_F Displacement.

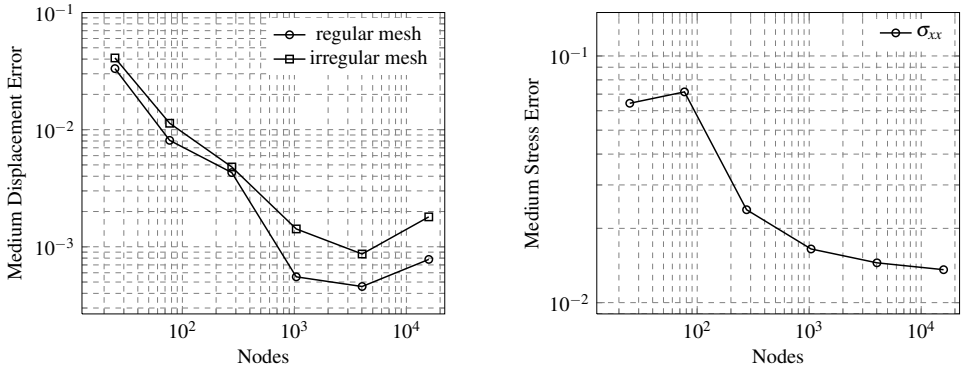

Figure 5.13: Square Plate with a Circular Hole: (a) Medium Displacement Error; (b) Medium Stress Error.

The study of the stress distribution along interest lines of the solid focused on the two edges with essencial boundary conditions. Therefore, figures 5.14(a) and 5.14(b) represent the evolution of the σ_{xx} and σ_{yy} stresses along the line $x = 0$, while figures 5.14(c) and 5.14(d) represent the evolution of the same stresses along the line $y = 0$.

It is clear that the RPIM solution replicates the analytical solution with great precision.

Figure 5.15 displays the displacement and stress fields across the whole domain. Even though the displacement fields are very smooth, the stress fields display small zones where the stress variations are slightly more abrupt.

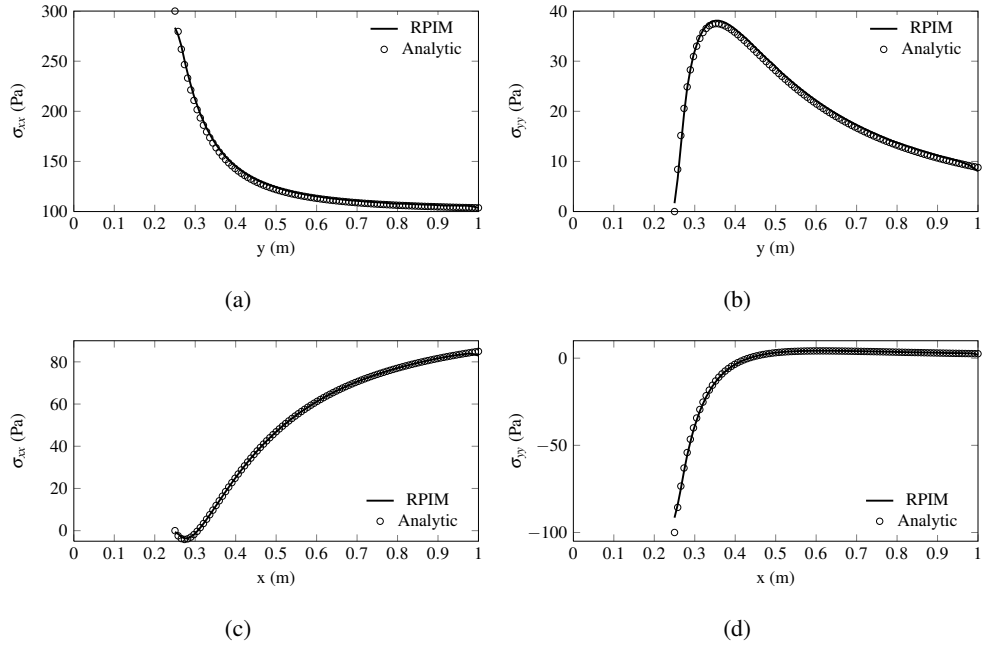

Figure 5.14: Square Plate with a Circular Hole: (a) σ_{xx} Stress Along $x = 0$; (b) σ_{yy} Stress Along $x = 0$; (c) σ_{xx} Stress Along $y = 0$; (d) σ_{xx} Stress Along $y = 0$.

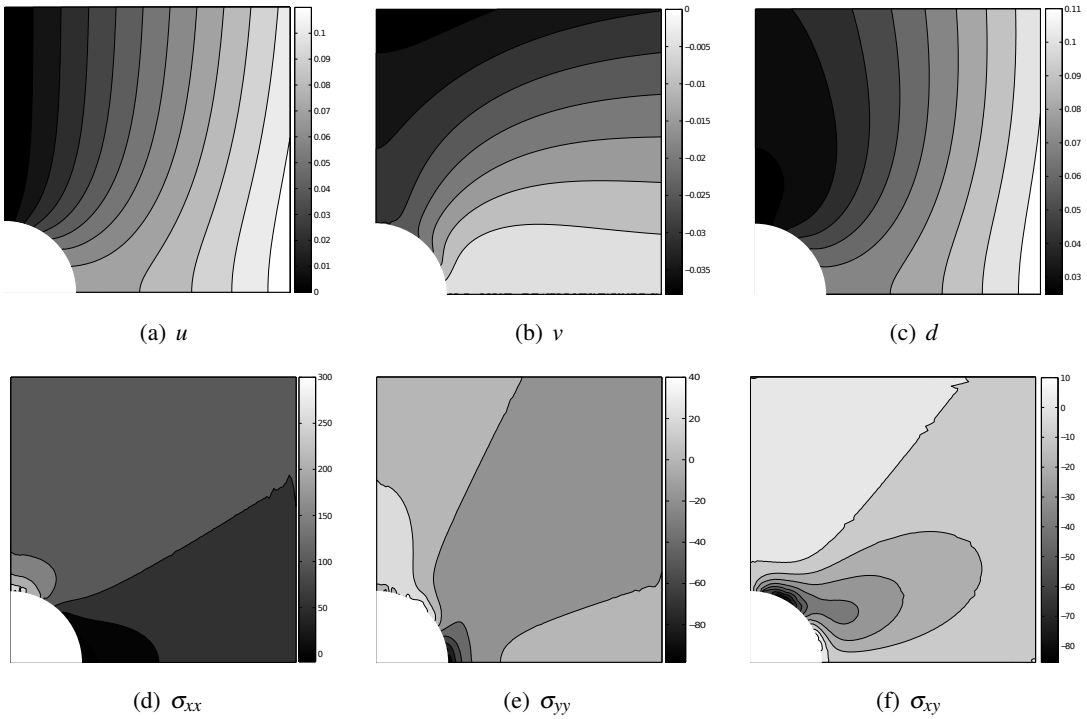

(a) u (b) v (c) d

(d) σ_{xx} (e) σ_{yy} (f) σ_{xy}

Figure 5.15: Square Plate with a Circular Hole: Displacement Field and Stress Field Distributions.

Chapter 6

Non Linear Applications

In this chapter several two dimensonal examples are analysed, in order to assess the performance of the nonlinear algorythm (KT0) with the RPIM. First, two well-known examples (cantilever beam and cook's membrane) are studied using a monotonic load. After that, the cantilever beam is analysed with two different kinds of cyclic load. The results obtained with the RPIM are compared with FEM solutions (either ABAQUS or ANSYS). The last example is the study of the trabecular bone and a polymer analogue.

6.1 Cantilever Beam

The cantilever beam problem represented in figure 6.1(a) is analysed. The domain was discretized in a regular mesh of 561 nodes, represented in figure 6.1(b). The dimensions and mechanical properties are also presented in figure 6.1(a).

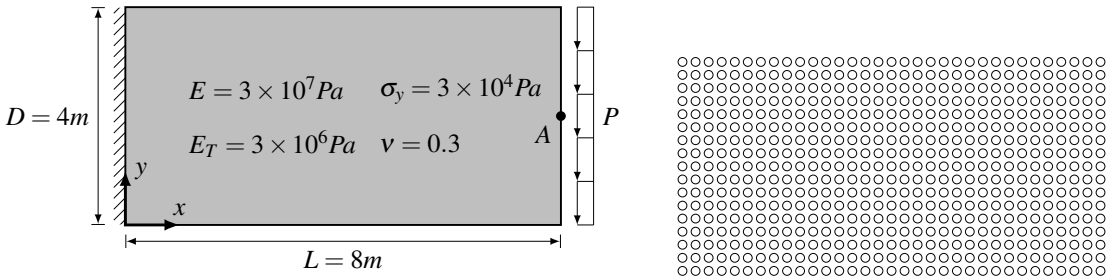

(a) (b)

Figure 6.1: Cantilever Beam: (a) Material and Geometric Conditions; (b) Regular 561 Node Mesh.

Figure 6.2 presents the vertical displacement evolution of point A (represented in figure 6.1(a)) with the increasing load P.

It is possible to observe that the RPIM fits the ANSYS solution (obtained from [31]) perfectly.

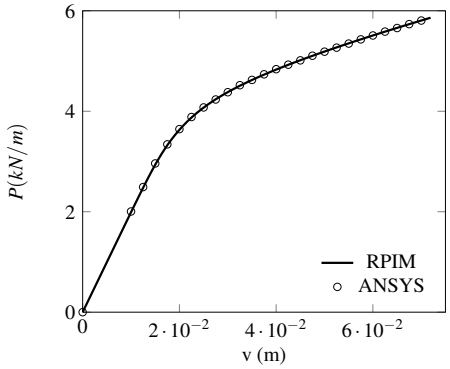

Figure 6.2: Cantilever Beam: v Displacement

In figure 6.3, the normal stress (σ_{xx}) distributions along the clamped edge ($x = 0$) for different values of the applied load are presented.

The results show that the RPIM solution is very close to the ANSYS solution over all the levels of applied load presented.

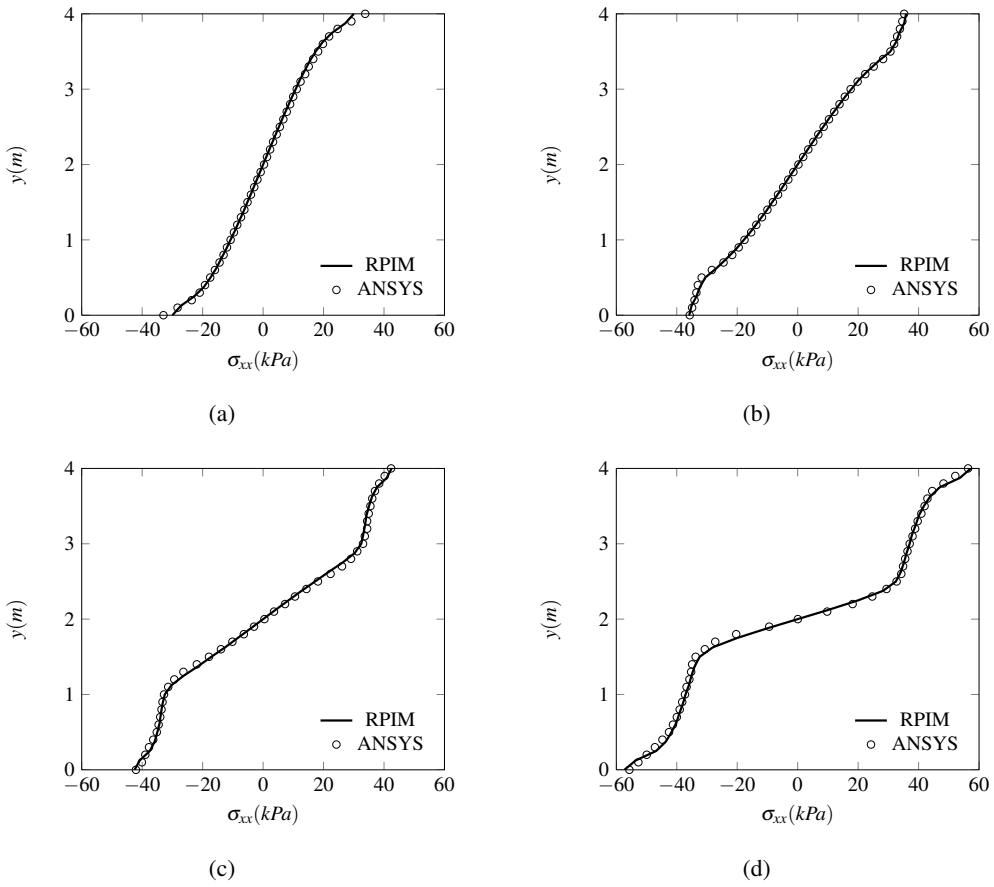

Figure 6.3: The Cantilever Beam: σ_{xx} Stress Distribution Along the Clamped Edge: (a) $P = 2.08kN/m$; (b) $P = 3.12kN/m$; (c) $P = 4.16kN/m$; (d) $P = 5.20kN/m$.

6.2 Cook's Membrane

The Cook's Membrane problem is presented on figure 6.4(a), along with the geometry, mechanical properties and boundary conditions. The domain was discretized in a regular mesh of 289 nodes, represented in figure 6.4(b).

The solutions obtained with the RPIM were compared with the solutions from ANSYS [31].

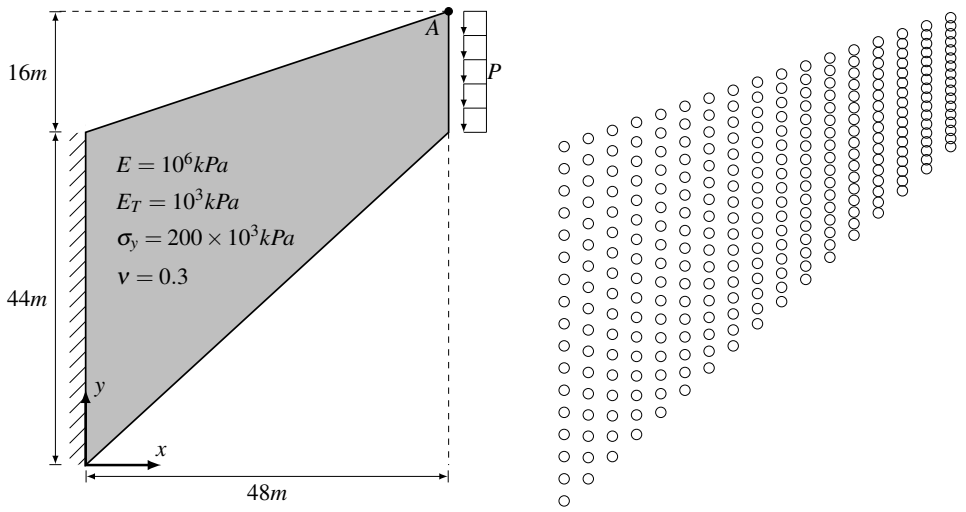

(a) (b)

Figure 6.4: Cook's Membrane: (a) Material and Geometric Conditions; (b) Regular 289 Node Mesh.

The horizontal and vertical displacements of point A are presented in figure 6.5(a) and figure 6.5(b), respectively. It is visible that the RPIM solution is very close to the ANSYS solution for both displacements.

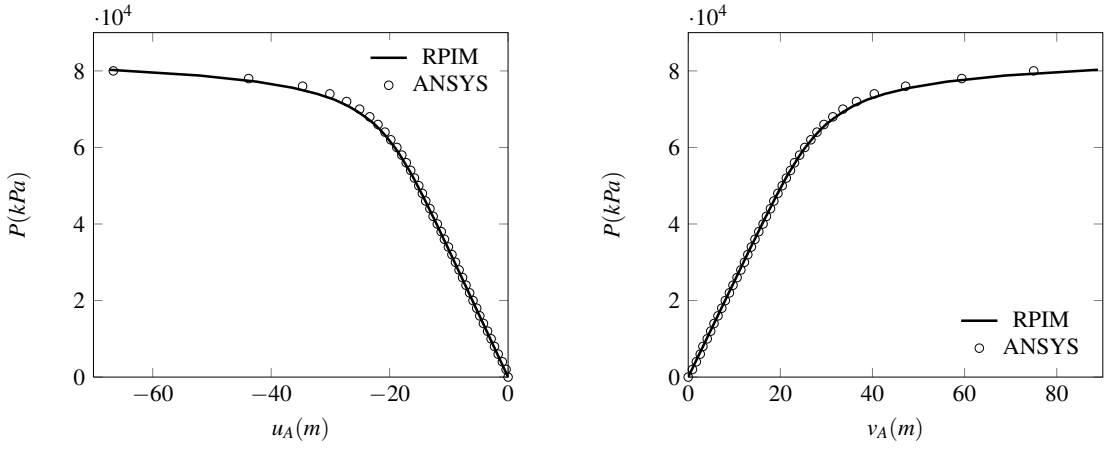

(a) (b)

Figure 6.5: Cook's Membrane: (a) u_A; (b) v_A.

Figure 6.6 shows the evolution of the normal stress σ_{xx} along the clamped edge of the cook's membrane, for increasing levels of the applied load P.

Similar to the displacement results, the relation between the RPIM and ANSYS solutions for the normal stress σ_{xx} is very close, apart from small local disturbances. As it would be expected, given the geometry and the type of loading, the top part of the clamped edge is the first to yeld, since it's there were the normal stresses are higher.

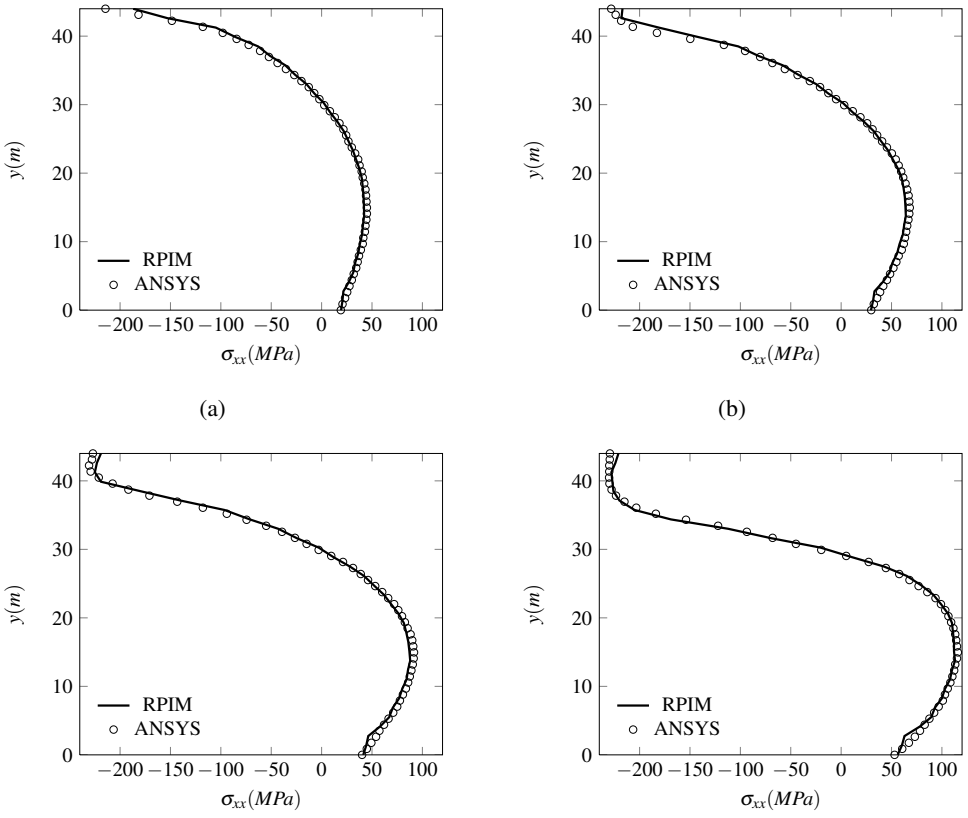

Figure 6.6: Cook's Membrane: σ_{xx} Stress Distribution Along the Clamped Edge: (a) $P = 3.10 \times 10^4 kN/m$; (b) $P = 4.75 \times 10^4 kN/m$; (c) $P = 6.35 \times 10^4 kN/m$; (d) $P = 8.00 \times 10^4 kN/m$.

The same analysis presented in figure 6.6 is shown in figure 6.7, now for the shear stress σ_{xy}. Although it is clear that the two solutions are not as close as on previous examples, specially for higher load values, the RPIM still performs fairly well when compared to the ANSYS solution.

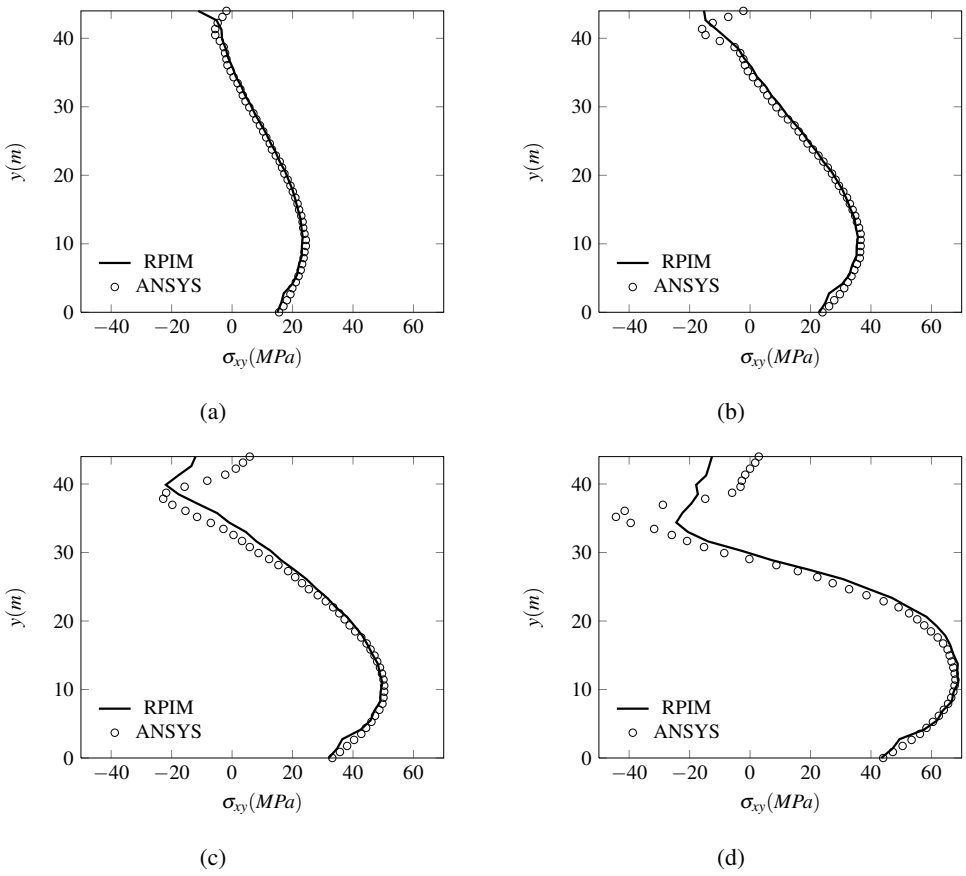

Figure 6.7: Cook's Membrane: σ_{xy} Stress Distribution Along the Clamped Edge: (a) $P = 3.10 \times 10^4 kN/m$; (b) $P = 4.75 \times 10^4 kN/m$; (c) $P = 6.35 \times 10^4 kN/m$; (d) $P = 8.00 \times 10^4 kN/m$.

6.3 Non Monotonic Loading

In this section, the classic elastoplastic analysis is extended to the case of the non monotonic loading pattern. The model used for this analysis is the cantilever beam, presented in figure 6.1(a). All the results obtained with the RPIM are compared with a finite element solution (ABAQUS). The number of nodes used in the finite element simulation is more than twice the number used in RPIM, and eight node elements are used.

Three different cases of loads are studied. In the first case, the load is increased until a certain level after the yield started. After this, the structure is fully unloaded, and the load is again incresead past the previous maximum load value.

The second load case is similar to the first, except that in the second case, the structure is unloaded and reload several times, instead of just one.

The vertical displacement of point A for the first load case is presented in figure 6.8, while figure 6.9 shows the same displacement for the second load case.

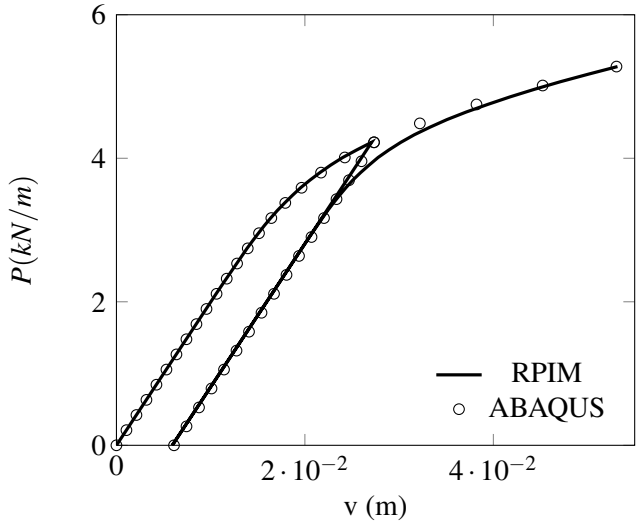

Figure 6.8: Non Monotonic Loading of Cantilever Beam: v_A Displacement for the First Load Case

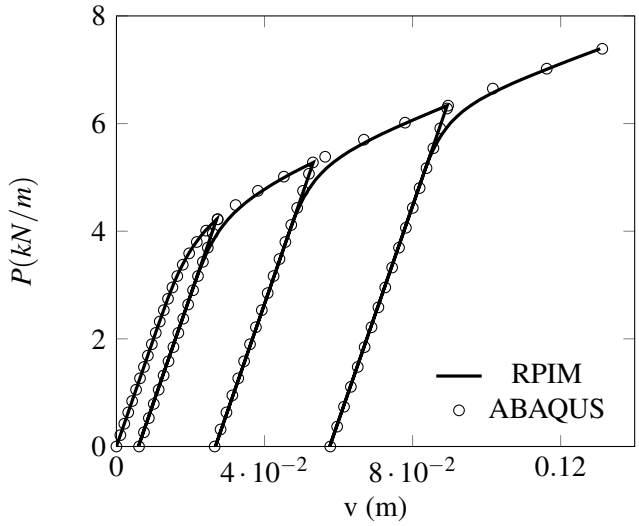

Figure 6.9: Non Monotonic Loading of Cantilever Beam: v_A Displacement for the Second Load Case

It is clear to observe from the two figures that the structure unloads and reloads following a line that is parallel to the initial elastic behaviour, as it would be expected.

It would be expected that, after being unloaded and reloaded, the structure would yield exactly in the same point it was before being unloaded (behaviour correctly reproduced by the ABAQUS solution) and continue the plastic evolution, as if the load never changed.

Although it is visible that in the RPIM solution, the structure yields sooner than it should, the relation between the two solutions is very good, since the RPIM solution quickly converges to the finite element solution.

In the third and final load case, everytime the structure is unloaded and reloaded, the direction of the load is reversed, i.e. the beam is subjected to a positive load, then it is unloaded and after that it is subjected to a negative load, and so on.

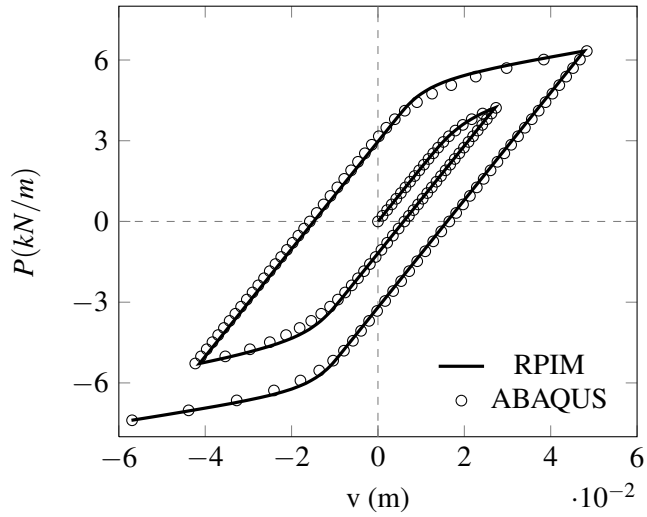

Figure 6.10: Non Monotonic Loading of Cantilever Beam: v_A Displacement for the Third Load Case

Figure 6.10 shows the displacement of point A for the third load case. Unlike the two previous cases, the relation between the RPIM and the ABAQUS solutions ir very close, and the early yielding issue is not present.

6.4 Trabecular Bone

In this section the trabecular bone is analysed. Figure 6.11 shows the experimental results obtained by [45] for the confined square test. The geometry, load and boundary conditions used are presented in figure 6.12.

By observing the experimental data, it is visible that the trabecular bone's mechanical behaviour can be represented by a bilinear material model, at least until densification occurs, as shown in figure 6.11.

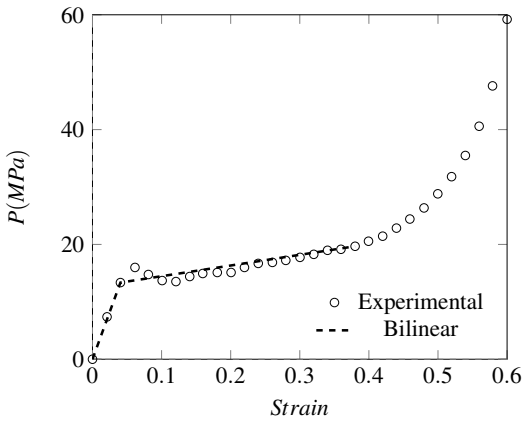

Figure 6.11: Trabecular Bone: Experimental Results and Bilinear Model

The mechanical properties of the bilinear model are presented in figure 6.12 (the Poisson's ratio is obtained from the literature [45]).

For the RPIM analysis, a 289 node mesh was used, similar to the one represented in figure 5.1(a).

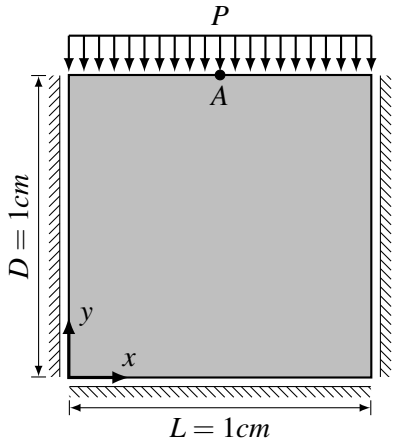

	Trabecular Bone	**Polymer Analogue**
	$E = 350.5MPa$	$E = 147.6MPa$
	$E_T = 18.6MPa$	$E_T = 3.6MPa$
	$\sigma_Y = 13.4MPa$	$\sigma_Y = 5.6MPa$
	$\nu = 0.16$	$\nu = 0.20$

Figure 6.12: Trabecular Bone and Polymer Analogue: Material and Geometry Conditions

The strain of point A is presented in figure 6.13. It is visible that, even though the RPIM presents a slightly stiffer behaviour than the bilinear model, the relation between the two is fairly good.

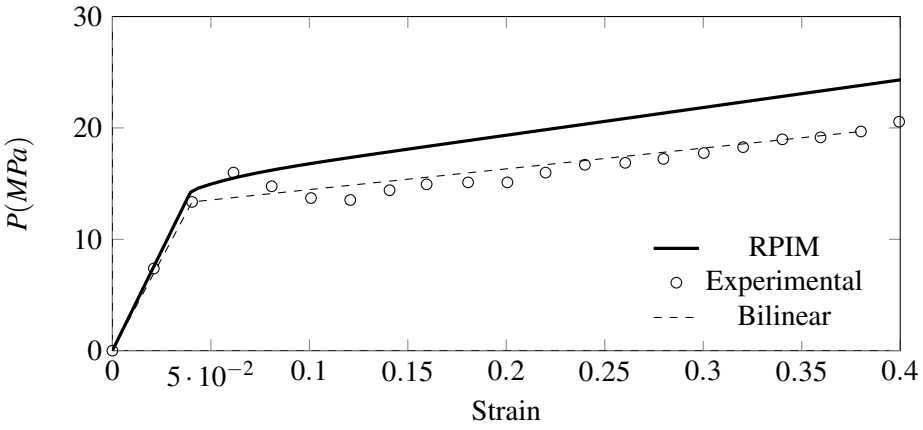

Figure 6.13: Trabecular Bone: ε_A Strain

A trabecular bone analogue material is also studied. Figure 6.14 shows the experimental results obtained for the celular rigid polyurethane (PU) foam. The same boundary and load conditions are applied. Once again, a bilinear model is defined to simulate the foam material until densification. The material properties for the bilinear model are presented in figure 6.12.

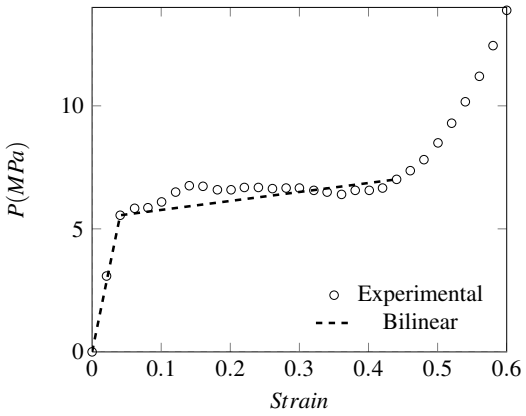

Figure 6.14: Polymer Foam: Experimental Results and Bilinear Model

Figure 6.15 shows the strain of point A for the PU foam analysis. The results are very similar to the trabecular bone study. Although the RPIM solution is slightly stiffer, the relation between the RPIM solution and the bilinear model is fairly good.

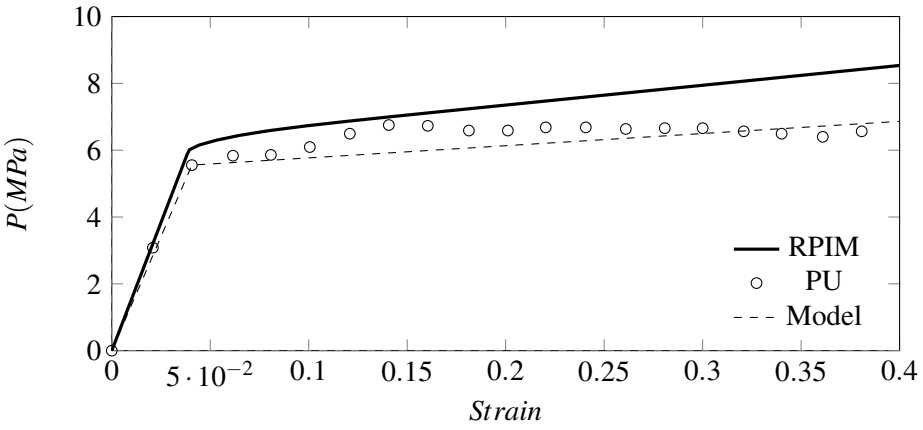

Figure 6.15: Polymer Foam: ε_A Strain

6.5 Cortical Bone

The final elastoplastic example is the study of the trabecular bone. Figure 6.17 shows the bilinear models of the cortical bone. These were obtained through the analysis of experimental tests [46]. The tests were performed at different speed levels, and figure 6.17 presents the ones performed with the highest and lowest speeds.

The geometry, boundary and load conditions, as well as the mechanical properties of the bilinear models are presented in figure 6.16. The model has the same dimensions as the model for the trabecular bone, but in this case, the base is clamped and the sides are free.

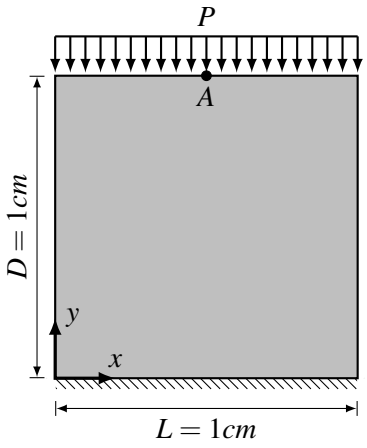

	High Speed	**Low Speed**
	$E = 18.5GPa$	$E = 11.6GPa$
	$E_T = 2.2GPa$	$E_T = 0.95GPa$
	$\sigma_Y = 128.9MPa$	$\sigma_Y = 79.3MPa$
	$\nu = 0.36$	$\nu = 0.36$

Figure 6.16: Cortical Bone: Material and Geometry Conditions

The RPIM solution for the strain of point A is presented in figure 6.17. It is visible that the relation between the RPIM solution and the bilinear model is very close, for both the slow and high speed models.

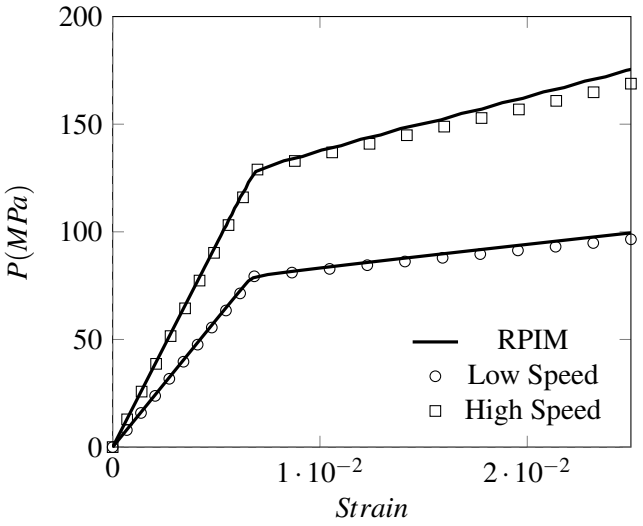

Figure 6.17: Cortical Bone: ε_A Strain for High and Low Speed

Chapter 7

Conclusions and Future Works

In this work, the RPIM was applied to the study of non-linear problems, with both monotonic and non monotonic loads.

First, several linear elastic examples were analysed. With the results obtained from these tests, it is possible to conclude that the RPIM solutions are very close to the exact problem solutions, even with relatively small meshes. The displacement and stress fields obtained are accurate and very smooth. Also, the use of regular or irregular meshes has little or no influence in the final solution.

The RPIM was then applied to elastoplastic problems. Regarding the monotonic load cases, the results obtained for the displacement are extremely close to the FEM solution, with an equal or smaller mesh. The stress results are also very close to the FEM solution, however in some cases the relation is slighty different. From the analysis of the non monotonic load cases, it was concluded that, even though the model yields a little sooner than it is supposed to when the structure is reloaded in the same direction, the RPIM solution is very close to the ABAQUS solution.

The final application was the trabecular and cortical bone study. For the trabecular bone (and polymer analogue), the RPIM solution is slightly stiffer than the bilinear model, although the relation between the two is fairly good. The results obtained for the cortical bone are very close to the bilinear model, for both the high speed and low speed cases.

In general, the elastoplastic results show that the non-linear solution algorithm, as well as the procedure for the stress returning were successfully implemented in the RPIM.

Even though the RPIM has good accuracy and produces smooth stress fields, its main disadvantage when compared to the FEM is the high computational cost.

Several additions could enhance this work, such as:

- The inclusion of large deformations;
- The inclusion of dynamic analysis;
- The inclusion of new hardening rules, namely the kinematic hardening rule, in order to reproduce the Bauschinger effect with non monotonic loads;
- The study of other modified Newton-Raphson methods (for example KT1), as well as the study of new non-linear algorithms, such as the arc-length method, to reproduce structural instabilities, namely the "snap-through" and the "snap-back" phenomena;

References

[1] B. Nayroles, G. Touzot, and P. Villon, "Generalizing the finite element method: Diffuse approximation and diffuse elements," *Computational Mechanics*, vol. 10, pp. 307–318, 1992.

[2] T. Belytschko, Y. Krongauz, D. Organ, M. Fleming, and P. Krysl, "Meshless methods: an overview and recent developments," *Computer Methods in Applied Mechanics and Engineering*, vol. 139, pp. 3–47, 1996.

[3] P. W. Randles and L. D. Libersky, "Smoothed particle hydrodynamics: Some recent improvements and applications," *Computer Methods in Applied Mechanics and Engineering*, vol. 139, pp. 375–408, 1996.

[4] V. P. Nguyen, T. Rabczuk, S. Bordas, , and M. Duflot, "Meshless methods: A review and computer implementation aspects," *Mathematics and Computers in Simulation*, vol. 79, pp. 763–813, 2008.

[5] J. J. Monaghan, "Smoothed particle hydrodynamics: Theory and applications to non-spherical stars," *Monthly Notices of the Astronomical Society*, vol. 181, pp. 375–389, 1977.

[6] L. D. Libersky and A. G. Petschek, "Smoothed particle hydro-dynamics with strength of materials," in *The Next Free Lagrange Conference*, pp. 248–257, 1991.

[7] T. Belytschko, Y. Y. Lu, and L. Gu, "Element-free galerkin methods," *International Journal for Numeric Methods in Engineering*, vol. 37, pp. 229–256, 1994.

[8] P. Lancaster and K. Salkauskas, "Surfaces generation by moving least squares methods," *Mathematics of Computation*, vol. 37, pp. 141–158, 1981.

[9] W. K. Liu, S. Jun, S. Li, J. Adee, and T. Belytschko, "Reproducing kernel particle methods for structural dynamics," *International Journal for Numeric Methods in Engineering*, vol. 38, pp. 1655–1679, 1995.

[10] Z. T. Atluri, "A new meshless local petrov–galerkin (mlpg) approach in computational mechanics," *Computational Mechanics*, vol. 22(2), pp. 117–127, 1998.

[11] L. M. J. S. Dinis, R. M. N. Jorge, and J. Belinha, "Analysis of 3d solids using the natural neighbour radial point interpolation method," *Computer Methods in Applied Mechanics and Engineering*, vol. 196, pp. 2009–2028, 2007.

[12] K. M. Liew, X. Zhao, and A. J. M. Ferreira, "A review of meshless methods for laminated and functionally graded plates and shells," *Composite Structures*, vol. 93, pp. 2031–2041, 2011.

[13] G. Liu and Y. Gu, "A point interpolation method for two-dimensional solids," *International Journal for Numeric Methods in Engineering*, vol. 50, pp. 937–951, 2001.

[14] J. Wang, G. Liu, and Y. Wu, "A point interpolation method for simulating dissipation process of consolidation," *Computational Methods in Applied Mechanics and Engineering*, vol. 190, pp. 5907–5922, 2001.

[15] J. Wang and G. Liu, "A point interpolation meshless method based on radial basis functions," *International Journal for Numeric Methods in Engineering*, vol. 54, pp. 1623–1648, 2002.

[16] J. Wang and G. Liu, "On the optimal shape parameters of radial basis functions used for 2-d meshless methods," *Computational Methods in Applied Mechanics and Engineering*, vol. 191, pp. 2611–2630, 2002.

[17] J. Braun and M. Sambridge, "A numerical method for solving partial differential equations on highly irregular evolving grids," *Nature*, vol. 376, pp. 655–660, 1995.

[18] N. Sukumar, B. Moran, A. Semenov, and V. Belikov, "Natural neighbour galerkin methods," *International Journal for Numeric Methods in Engineering*, vol. 50, pp. 1–27, 2001.

[19] R. Sergio, S. Idelsohn, E. Onate, N. Calvo, and F. D. Pin, "The meshless finite element method," *International Journal for Numeric Methods in Engineering*, vol. 58, pp. 893–912, 2003.

[20] J. Belinha, L. M. J. S. Dinis, and R. M. N. Jorge, "The natural radial element method," *International Journal for Numerical Methods in Engineering*, vol. 93, pp. 1286–1313, 2013.

[21] J. Belinha, L. M. J. S. Dinis, and R. M. N. Jorge, "Composite laminated plate analysis using the natural radial element method," *Composite Structures*, vol. 103, pp. 50–67, 2013.

[22] J. Belinha, "The radial point interpolation meshless method introduction course." Institute of Mechanical Engineering - FEUP, September 2011.

[23] Y. T. Gu, "Meshfree methods and their comparisons," *International Journal of Computational Methods*, vol. 2(4), pp. 477–515, 2005.

[24] O. C. Zienkiewicz, *The Finite Element Method*. McGraw-Hill, 1989.

[25] K. J. Bathe, *Finite Element Procedures*. Prentice-Hall: Englewood Cliffs, 1996.

[26] E. J. Kansa, "A scattered data approximation scheme with applications to computational fluid-dynamics," *Computers and Mathematics with Applications*, vol. 19, pp. 127–161, 1990.

[27] J. Belinha, "Elasto-plastic analysis considering the element free galerkin method," Master's thesis, Faculdade de Engenharia da Universidade do Porto, 2004.

[28] G. R. Liu, "A point assembly method for stress analysis for two-dimensional solids," *International Journal of Solid and Structures*, vol. 39, pp. 261–276, 2002.

[29] R. L. Hardy, "Theory and applications of the multiquadrics - biharmonic method (20 years of discovery 1968-1988)," *Computers and Mathematics with Applications*, vol. 19, pp. 163–208, 1990.

[30] J. Belinha, R. M. N. Jorge, and L. M. J. S. Dinis, "Bone tissue remodelling analysis considering a radial point interpolator meshless method," *Engineering Analysis with Boundary Elements*, vol. 36, pp. 1660–1670, 2012.

[31] S. F. Moreira, "Elastoplastic analysis using the natural neighbour radial point interpolation method," Master's thesis, Faculdade de Engenharia da Universidade do Porto, 2013.

[32] S. Moreira, J. Belinha, L. M. J. S. Dinis, and R. M. N. Jorge, "Analysis of laminated beams using the natural neighbour radial point interpolation method (nnrpim)," *Revista Internacional de Métodos Numéricos para Cálculo y Diseño en Ingeniería*, p. in press, 2013.

[33] G. R. Liu and S. S. Quek, *The Finite Element Method: A Pratical Course*. Butterworth-Heinemann, 2003.

[34] S. Timoshenko and J. N. Goodier, *Theory of Elasticity*. McGraw-Hill, 1951.

[35] J. F. S. Gomes, *Mecânica dos Sólidos e Resistência dos Materiais*. Porto: Edições INEGI, 2009.

[36] G. R. Liu, *Meshfree Methods: Moving Beyond the Finite Element Method*. CRC Press, New York, 2000.

[37] J. N. Reddy, *Applied Functional Analysis and Variational Methods in Engineering*. McGraw-Hill International Edition, 1986.

[38] O. C. Zienkiewicz and R. L. Taylor, *The Finite Element Method for Solid and Structural Mechanics*. Elsevier Butterworth-Heinemann, 2005.

[39] J. A. O. P. Belinha, *The Natural Neighbour Radial Point Interpolation Method*. PhD thesis, Faculdade de Engenharia da Universidade do Porto, 2010.

[40] J. Chakrabarty, *Theory of Plasticity*. McGraw-Hill International Edition, 1987.

[41] R. Hill, *The Mathematical Theory of Plasticity*. Oxford University Press, 1950.

[42] D. R. J. Owen and E. Hinton, *Finite Elements in Plasticity: Theory and Practice*. Pineridge Press Limited, 1980.

[43] M. A. Crisfield, *Non-linear Finite Element Analysis of Solids and Structures*. John Wiley Sons, 2000.

[44] J. Belinha, L. M. J. S. Dinis, and R. M. N. Jorge, "The natural radial element method," *International Journal for Numerical Methods in Engineering*, p. Published online in Wiley Online Library, 2012.

[45] N. Kelly and J. P. McGarry, "Experimental and numerical characterisation of the elasto-plastic properties of bovine trabecular bone and a trabecular bone analogue," *Journal of the Mechanical Behavior of Biomedical Materials*, vol. 9, pp. 184–197, 2012.

[46] A. N. Natali, E. L. Carniel, and P. G. Pavan, "Constitutive modelling of inelastic behaviour of cortical bone," *Medical Engineering Physics*, vol. 30, pp. 905–912, 2008.

REFERENCES